Preservation of Organic Carbon in Dolomitized Cambrian Stromatolites and Implications for Microbial Biosignatures in Diagenetically Replaced Carbonate Rock

ASHLEY E. MURPHY[a*], SCOTT T. WIEMAN[b,c,d], JULIANE GROSS[e], JENNIFER C. STERN[c], ANDREW STEELE[f], MIHAELA GLAMOCLIJA[a]

[a]*Rutgers University, Department of Earth and Environmental Sciences, 101 Warren St, Smith Hall – Room 135, Newark, NJ, 07102 (*corresponding author e-mail: ashley.murphy@rutgers.edu)*

[b]*Center for Space Sciences and Technology, University of Maryland, Baltimore, MD 21250, USA*

[c]*Planetary Environments Laboratory, NASA Goddard Space Flight Center, Greenbelt, MD 20771, USA*

[d]*Center for Research and Exploration in Space Science and Technology, NASA Goddard Space Flight Center, Greenbelt, MD 20771, USA*

[d]*Department of Earth and Planetary Sciences, Rutgers University, New Brunswick, NJ 08854, USA*

[f]*Geophysical Laboratory, Carnegie Institution of Washington, Washington, DC, 20015, USA*

ABSTRACT

Stromatolites have been a major focus in the search for ancient microbial biosignatures, however, the organic carbon biosignatures of dolomitized stromatolites have not yet been fully characterized and correlated with their dolomitizing conditions. The lack in detailed dolomitic stromatolite studies is likely because dolomitization rarely preserves microbial morphology, which hampers the characterization of fossils' biogenicity, syngenicity and indigeneity to their host rock. The Cambrian Allentown Formation in New Jersey, USA is an excellent example of dolomitized stromatolites and thrombolites containing diagenetically modified microbial biosignatures. Based on XRD and EPMA data, the dolomite is near- to stoichiometric, and poorly to well ordered. The outcrop underwent early dolomitization in a marginal-marine setting and later burial diagenesis resulting in multi-generational dolomite formation: (1) The microspar dolomite formed by early diagenetic replacement at or near the surface, that produced finely crystalline dolomite, (2) The zoned dolomite formed penecontemporaneously with the microspar phase as rhombohedral crystals by infilling primary pore spaces within the microspar matrix. The rhombic crystals continued to grow outward in alternating stages of Fe-enriched and -depleted fluids, which were preserved in zoned rims and revealed by cathodoluminescence, and (3) The saddle dolomite formed during late stage deep burial with Fe- and Mn-rich fluids, and occurs as a void-filling, high-temperature phase. Organic carbon, characterized using confocal Raman microscopy, has exclusive distribution within the microspar dolomite, and the D and G bands' characteristics reveal similar style thermal alteration as host rock, indicating that the mapped organic carbon is indigenous and syngenetic with the Cambrian carbonates. The findings presented in this study reveal organic matter found within microspar of various dolomitized facies deriving from different pools of organic carbon. This study sheds light on biosignatures in secondary dolostones and may aid biosignature detection in older carbonate rocks on Earth and Mars.

Keywords: dolomitization, Cambrian stromatolites, organic carbon, biosignatures, burial diagenesis

1. INTRODUCTION

Stromatolites are microbially mediated sedimentary structures that record the oldest forms of life on Earth (Barghoorn and Tyler, 1965; Grotzinger and Knoll, 1999; Allwood et al., 2006). These ancient carbonate structures have drawn a significant focus of geobiology and astrobiology research because of their ability to archive the interactions of biological, physical, and chemical processes (e.g., Hoffman, 2013), and for that reason stromatolites provide an invaluable reference to Earth's past. A complication in the reconstruction of these structures derives from the fact that, as any other rock and fossil, stromatolites undergo diagenesis over time, which alters original biological signatures (biosignatures), including chemical (e.g., organic carbon) and physical (e.g., cellular morphology) evidence, making reconstruction of original materials of even the best-preserved stromatolites debatable.

The most common diagenetic changes in stromatolites are silicification and dolomitization, which involve the replacement of original calcium carbonate ($CaCO_3$) by silica (SiO_2) during silicification and magnesium (Mg^{2+}) in dolomitization. Silicification during early diagenesis leads to the exceptional preservation of original textures, microfossils, and organic chemistry, which are leading indicators in the characterization of biogenicity, indigeneity, and syngenicity (Knoll et al., 1988; Buick, 1990; Grotzinger and Knoll, 1999; Van Kranendonk et al., 2003; Sugitani et al., 2007; Schopf and Kudryavtsev, 2012; Braiser et al., 2015). Unlike silicification, dolomitization commonly results in the loss of microbial morphology (Schopf, 1999; Bartley et al., 2000), making the characterization of syngenetic and indigenous biosignatures more difficult (Grotzinger and Rothman, 1996). Dolomite [$CaMg(CO_3)_2$] may form during deposition (as primary dolomite) or post-deposition (secondary dolomite) from various fluid chemistries and temperatures (Machel, 1978; Machel, 2004; Guido et al., 2018). The fate of organic matter preserved under such a wide variety of conditions is yet to be properly evaluated.

Although the dolomitization process may be destructive to original stromatolitic textures and compositions, studies of microfossils in dolomitic stromatolites have been reported. These studies interpreted the investigated dolomitic stromatolites as formed by primary dolomite precipitation (Rao et al., 2003; Ayllón-Quevedo et al., 2007; Sanz-Montero et al., 2008; Calça et al., 2016). The microfossils characterized in these primary dolomitic structures are preserved exclusively in silica (Ayllón-Quevedo et al., 2007; Sanz-Montero et al., 2008; Calça et al., 2016) and sulfur-rich mineral phases (Lindtke et al., 2011). The effects of secondary dolomitization on the preservation of organic material remain largely unexplored. Secondary dolomitization may occur in a wide range of environments from the surface to deep burial (several km depths) settings (Machel, 1978), under different temperatures and pressures, and as such provides a range of settings that could be conducive to the long-term preservation of the organics.

The lack of detailed insight into the preservation processes of organic matter, or biosignatures in general, within dolomitized carbonate lithologies is further complicated when applied to astrobiology. Carbonate lithologies are a recognized astrobiology target for Mars exploration (Cady et al., 2003; Summons et al., 2011; D'Elia et al., 2017). The primary science goal of the Mars 2020 mission is to determine whether life existed on Mars by seeking signs of extinct life in the rock record (Mustard et al., 2013; Williford et al., 2018). In February 2021, the Mars 2020 Perseverance rover will land in Jezero Crater, an ancient paleolake (~4-3.5 Ga) with a diverse suite of carbonate-bearing terrains, including those with Mg/Ca compositions similar to terrestrial dolomites (Horgan et al., 2020). Although the origin of the magnesium carbonates identified is still uncertain (Ehlmann et al., 2008; Goudge et al., 2015), the crater may contain lacustrine carbonate deposits, which are habitable environments on Earth that provide the potential for biosignature preservation (Horgan et al., 2020). Terrestrial analogs of ancient magnesium carbonates, such as dolomite-rich rocks, are important to expand our understanding of biosignature preservation in dolomite lithologies, and to facilitate the search for potential biosignatures in Martian magnesium carbonates.

On Earth, characterizing the effects of secondary dolomitization on microbial fossil preservation is critical for interpreting traces of early life in the geological record. The syngenicity and indigeneity of this type of fossilization in the geologic record can only be comprehensively examined after the degree of alteration of the host rock has been characterized and evaluated against that of the biologic remains (Buick, 1990; Braiser et al., 2004). Hence in this paper, we contrast the host rock alterations with the organic carbon contained within the Formation. The measurements of whole rock and high-resolution in situ analysis of the three dolomite crystal phases from the Cambrian Allentown Formation are used to characterize the dolomitization setting. Confocal Raman spectroscopy is used to determine the spatial association of organic carbon to minerals and their alteration. Finally, the results are used to evaluate the level of diagenetic alteration that has affected the outcrop, and the effect that such alteration had on the preservation of the organic carbon.

2. GEOLOGIC SETTING

2.1. Regional geology and sedimentology

The Late Cambrian (515-500 Ma) Allentown Formation (Weller, 1903; Howell, 1945; Harris et al., 1995; Dalton et al., 2014), commonly referred to as Allentown Dolomite, is part of the Kittatinny Supergroup (542-443 Ma). The Kittatinny Supergroup is a northeast trending lithostratigraphic unit (Fig. 1) that records the formation of the eastern Laurentian (ancient North American landmass) passive margin, when the deposition of shallow-water carbonates prevailed. Paleoreconstruction of the area shows Laurentia positioned below the equator and rotated approximately 90° clockwise from its current orientation (Blakey, 2016). During the Cambrian, sediments from eroding inland rocks were transported by streams to the coast and deposited on the shallow shelf (Miller, 1941; Dalton et al., 2014). The paleoenvironment has been interpreted as a shallow subtidal to supratidal setting resulting in the deposition of limestones that have subsequently dolomitized (Miller, 1941; Stead and Kodama, 1984; Dalton et al., 2014).

In the 1950s, the Allentown was divided into two members: the Limeport (bottom) and Allentown Members (top) (Drake Jr., 1965). This distinction was made in older literature because the lower Limeport Member contains numerous ‘cryptozoan’ (hereafter referred to as stromatolites) of various morphologies, including large domes with convex-shaped laminae, wavy beds, and small domes of laterally linked laminae (Drake Jr., 1965). Previous geologic mapping of the Allentown Formation reveals cyclic bedding (from oldest to youngest) as follows: textureless dololutite (<0.0039 mm grain size), dolarenite (0.0625-2 mm), oolitic dolarenite (0.0625-2 mm), dolorudite (>2 mm), cryptozoan (stromatolitic) dolomite, and desiccation dolorudite (>2 mm) (Drake Jr., 1965). These inversely graded bedding cycles suggest a regression sequence. Individual bedding cycles range in thickness from ~2 to 10 m, and the entire formational sequence measures up to 580 m thick (Drake Jr., 1965; Monteverde, 1992).

2.2. Study area

The study area in Hamburg, New Jersey, USA, includes 40 m of uplifted dolostone (dolomitic carbonate rock), tilted 44° NW. Exposure along the southwestern side of the outcrop (Figs 2, 3) allows for measurements of bedding thickness that are elsewhere inexact due to glacially polished rock surfaces. Along the longest transect, the outcrop is 100 m long with extensive vegetation cover that limits correlation between the northeast and southwest parts of the outcrop (Fig. 3). The southwest side of the outcropping does not contain microbial structures, but the transect analyzed in the middle of the outcropping area (Fig. 3) contains stromatolites and thrombolites. The bottom of the transect is ~13 m of fine-grained, grey dolosiltite intercalated with iron oxidized dissolution seams that are weathered black in outcrop (Fig. 2B). The occurrence of thrombolites (microbially mediated clotted structures) is marked by a brown wavy layer of ~1 cm thick laminae (Fig. 2C). The thrombolites are overlain by small (≤5 cm) round stromatolite heads (Fig. 2D, E) that continue to occur periodically in overlying strata for ~20 m. Massive oolitic dolarenite (Fig. 2F) is situated above the stromatolite heads for ~11 m. The oolitic grainstone is overlain by ~13 m of dolosiltite with numerous beds of high energy, storm deposit features of rip-up clasts (linear feature) (Fig. 2G), edgewise conglomerates (Fig. 2H), and jumbled intraclasts (non-linear feature) (Fig. 2I). These beds co-occur with coarse-grained dolomite-filled vugs (≤9 mm) (Fig. 2J). Large (≤30 cm) domal stromatolites, as well as intraclasts and collapse breccia are observed at the top of the formation (Fig. 2K). The northeast side of the outcrop reveals the convex up structure of the domes (Fig. 2L). Mudcracks (continuous, polygonal) are situated above the large domal stromatolites (Fig. 2M) and syneresis cracks (discontinuous, sinuous) are observed southwest of the stromatolites (Fig. 2N). Wavy stylolites parallel to bedding are found throughout the formation (Fig. 2O). Chert occurs as black lenses or thin layers (~1 cm) throughout the formation (Fig. 2P). This bedding sequence corresponds to marine regression peritidal sequence (Fig. 1C).

3. MATERIALS AND METHODS

3.1. Sampling strategy

Samples (n = 22) were collected from 2017 to 2020 in Hamburg, New Jersey, USA. The sampling strategy included twenty-two different sampling points, from bottom to top of the formation, while targeting obvious stromatolitic morphologies and significant changes in strata texture or appearance (Fig. 3). Sampled transects are marked A and B (Fig. 3) and the starting letter of each sample name (Table 1) corresponds to the transect where the sample was collected, samples labeled *12b-d are not part of either transect but rather the samples that exhibited characteristic textures and were collected at sides of the transects. Table 1 lists samples from bottommost (*12d) to the topmost bedding layers (A18) and what samples were included in which analysis in this study. Hand-sized samples were collected in an organically clean manner to avoid contamination by using gloves to handle samples that were wrapped in sterile aluminum foil and placed in canvas bags. Subsampling was performed in the laboratory using a diamond blade saw and DI water to cut away outer rock layers from the interior areas that were later used for analyses.

3.2. Petrographic and mineralogical analyses

Petrographic analyses of 14 texturally different layers were used to describe the stromatolites and associated dolostone. The petrographic study involved plane polarized and cross polarized light inspection of thin sections for textural and mineral identification, as well as to target regions of interest for further spectroscopy. The detection of minor mineral phases was performed by scanning electron microscopy with energy dispersive X-ray spectroscopy (SEM/EDS) at Rutgers University using a Hitachi S-4800 operating at 15 to 20 kV and 12 to 15 uA, equipped with an Apollo X EDAX.

Powder X-ray diffraction (XRD) of whole rock samples was used to determine dominant mineral assemblages in 21 samples. The equipment used at Rutgers University was a Bruker D8 with a Cu-Kα radiation. Operational settings were 40 kV, 25 mA. XRD spectra were collected over the 2ϴ range of 5-75° and with a step size of 0.02° or 0.04° and a count time of 48 or 115 s per step, respectively. Identification of peak patterns was performed in DIFFRAC.suite. Eva V3.1 software using the International Center for Diffraction Data database (version PDF2013).

Backgrounds were subtracted before calculating d-spacing values. Stoichiometry was calculated by taking the 2Θ value of the d_{104} peak, and converting the 2Θ to d-spacing using Bragg's Law (Bragg and Bragg, 1913), and lastly, using the equation in Lumsden (1979) which relates the d-spacing of the d_{104} peak to mol% of $CaCO_3$. The equation derived by Lumsden (1979) can result in ≤ 3 mol% $CaCO_3$ inaccuracies (Reeder and Sheppard, 1984), and therefore this stoichiometric data was checked by electronprobe microanalysis data. The degree of cation ordering was calculated by the intensity ratio of the d_{015} and d_{110} peak (Graf and Goldsmith, 1956; Goldsmith and Graf, 1958). Reported values of dolomite stoichiometry and degree of cation order represent bulk sample averages only.

3.3. Geochemical analyses

$\delta^{13}C_{dolo}$ and $\delta^{18}O_{dolo}$ were analyzed via acidification of each powdered sample at 60°C using 85% H_3PO_4. Analyses were carried out on a GasBench II System (Thermo) coupled to a Delta V Plus isotope ratio mass spectrometer (IRMS) (Thermo) at NASA Goddard Space Flight Center. The bulk (n=16) and micro-drilled (n=7) samples were analyzed to determine the isotope ratios of dolomite. The micro-drilled samples were sampled from thin-section billets at Rutgers University using a Medenbach micro-drill in order to isolate microspar and saddle dolomite phases for comparison to the bulk rock, and to target the minimum and maximum temperature of formation. The bulk samples were analyzed in triplicate, and micro-drilled samples were analyzed in, at minimum, two replicates. Standards were run before, in the middle of, and after each run. Precision is based on reproducibility of NIST reference standard NBS-19 at ±0.05‰ for $\delta^{13}C_{dolo}$ and ±0.15‰ for $\delta^{18}O_{dolo}$. Isotopic values are reported relative to the Vienna Pee Dee Belemnite (VPDB).

Organic carbon abundance, nitrogen abundance, and $\delta^{13}C_{org}$ were determined using an Elemental Analyzer (Costech) coupled to a Delta V Plus IRMS (Thermo) at NASA Goddard Space Flight Center. Powdered samples were placed in ashed (500°C) glass vials. Sedimentary organic material was separated via dissolution in 6N HCl for approximately 48-96 hours. Insoluble material was allowed to settle before samples were carefully decanted and then left to dry. The complete dissolution of carbonates was verified using SEM/EDS microscopy. Dry insoluble material was scraped out of glass containers, weighed, and packed into tin capsules for analyses. Standards were analyzed periodically during each run to assess the precision of the measurements. Precision is based on reproducibility of reference standard USGS40 (glutamic acid) at ±0.07‰ for $\delta^{13}C_{org}$. Isotope values are reported relative to the Vienna Pee Dee Belemnite (VPDB) standard and total organic carbon as wt%. To calculate wt% organic carbon, the analyzed sample's weight was divided by its total weight (pre-dissolution) and multiplied by 100%. The residual % of organic carbon measured was then converted to TOC by the following equation:

$$\text{TOC} = ((\text{organic carbon measured}) * (\text{analyzed sample weight} / \text{initial sample weight})).$$

Qualitative elemental X-ray mapping (n=2) and cathodoluminescence (CL) mapping (n=9) was performed on thin sectioned samples with the JEOL Superprobe JXA-8200 at Rutgers University. Samples were chosen based on texturally different microscale features. Operating conditions were 15 kV accelerating voltage, 14 nA beam, focused beam diameter (~1 micron), a step size of 1 µm, and a dwell time of 30 ms. The Kα X-ray maps and CL maps were processed with the xCLent software at Rutgers University to create red, green, and blue (RGB) colored composite maps of the sample.

Quantitative electronprobe microanalyses (EPMA) of mineral composition were obtained on 7 samples with the JEOL Superprobe JXA-8200 at Rutgers University, to isolate each phase of dolomite. Operating conditions were 15 kV accelerating voltage, 15 nA beam current, and a beam diameter of 5 microns. Analytical standards were well-characterized synthetic oxides and minerals including Strontianite (Sr), Orthoclase (Si), Fayalite (Fe), Rhodonite (Mn), Calcite (Ca), ZnO (Zn), Dolomite (Mg). Data quality was ensured by analyzing secondary standard materials as unknowns. Average detection limits (in oxide wt%) are SrO = 0.03; MnO, SiO_2, FeO = 0.02; CaO, MgO = 0.01; and ZnO = 0.17. The average analytical errors for elements above detection limit are: Ca ~0.25%; Mg ~0.47%; Fe ~5.36%; and Mn ~46%. Stoichiometry (Mg/Ca) was calculated for each phase of dolomite. Stoichiometry was determined by converting the average elemental wt% of Mg and Ca for each dolomite phase to mol% Mg and Ca, where total percentage of Mg and Ca was normalized to 100.

3.4. Confocal Raman microscopy

Confocal Raman microscopy and spectroscopy was used for spot analyses and mapping of 14 thin sections and 8 unprocessed rock samples, to determine the organic carbon spatial distribution, associations with minerals, and to analyze the D and G bands (~1350 and 1600 cm^{-1}, respectively) characteristic Raman signal for the organic matter. Five thin sections were chosen for the final high-resolution analysis. These representative layers ranged across the top, middle, and bottom areas of the outcrop and include all lithological textures observed. This work was performed at Rutgers University with a WITec alpha300 equipped with a frequency-doubled Nd:YAG (532 nm) excitation laser. Operational settings were as follows: a 1 mV average laser intensity (range from 1-3 mV) to minimize laser-induced heating and to avoid structural modification of the samples, and a depth of 1-5 μm below the surface to was used to avoid surface contamination. Mapped areas were visually inspected by transmitted and reflected light microscopy for holes and cracks in the samples that may contain polishing grit, epoxy, or other contaminants related to sample handling that may interfere with the D and G band spectra. Samples that could not be unambiguously identified as unaffected by this type of contamination or were too friable for thin sectioning were not included in the final Raman data sets.

D and G bands were analyzed in two ways for data quality assessment, using 1) WITec Project FIVE+ software cluster analysis and, 2) WITec Project FIVE+ software Gaussian fitted background subtraction. The cluster method identifies variations in D and G band phases within a map, averages it, and displays a distribution map. Ten clusters of spectral variations were calculated from each map, and one to three were chosen from each mapped area after quality evaluations (signal-to-noise ratio, surface contamination, and interference bands from hematite were avoided after being inspected both visually and spectrally). The Gaussian fit method uses a Savitzky-Golay filter to smooth the graph before applying background subtraction using a Gaussian fit for both the G and D bands. The average D and G band peak centers are displayed on a distribution map where one to three spectral points, representative of different spectral trends, were hand selected. Maps were inspected for visual and spectral interferences as listed above in the cluster analysis method.

All spectra were normalized to facilitate comparison. Band intensities were normalized by taking the height of each band and dividing it by the most intense G band in the spectrum. Data collected from both methods were exported as ASCII files into Excel and used to calculate the Raman parameters of the D/G intensity ratio, peak area, and the Raman shifted peak position. A two-tailed, two-sample *T*-test ($p=0.05$) was applied to D and G spectral data to determine if variations within the bands were statistically different. The peak table exported from the WITec software was used to report the full width at half maximum (FWHM) for both D and G bands. Thermometry was calculated using the D1 band geothermometer from Kouketsu et al. (2014):

$$T(°C) = -2.15 * (FWHM\text{-}D1) + 478\ (\pm 30°C)$$

This widely used geothermometer was chosen due to the consistency of FWHM with temperature (Kouketsu et al., 2014) and the spectral characteristics of the Allentown's D and G peaks which do not exhibit an obvious D2 peak within the G peak.

4. **RESULTS**

4.1. Allentown petrology and mineralogy

4.1.1. Bulk mineralogy

Based on powder X-ray diffraction (XRD) (Fig. S1 in supplementary material) the mineralogy of the Allentown Formation is predominantly dolomitic with few ±1 to 40 cm thick, greyish-black chert lenses (Fig. 2P), and ~1 cm brown colored feldspathic carbonate layers (Fig. 2C) (samples A15, B15b, and A6, respectively). The feldspathic (orthoclase and microcline) carbonate layers occur as thin wavy layers or disk-shapes and are commonly observed along fractured bedding surfaces or at the top of microbial macrostructures. Results for stoichiometry and cation ordering are presented in Table 2. The average d-spacing of the dolomite d_{104} peak is 2.889 Å and ranges 2.854 – 2.894 Å (1σ = 0.009) for (n=20) samples. These d-spacings indicate that the stromatolite (A16) and thrombolite (A5) are stoichiometric (50.0 and 49.7 mol% $CaCO_3$, respectively). The sample B11 has low Mg-excess (49.3 mol% $CaCO_3$), and the cherty outlier (B15b) is 39.3 mol% $CaCO_3$, and the remaining samples range from 51-53 mol% $CaCO_3$ (Table 2). The 14 samples show low Ca-excess of <53 mol% $CaCO_3$, and 2 samples are 52.7 mol% $CaCO_3$. Reported values are derived from bulk rock measurements and therefore represent sample averages, which may include an error of up to 3 mol% $CaCO_3$ due to the Lumsden (1979) calculation used (Reeder and Sheppard, 1984). The average degree of cation order calculated by the d_{015}/d_{110} intensity ratio is 0.67 and ranges 0.36 – 0.99 ($1\sigma = 0.16$) for (n=18) samples. The range of cationic ordering ratios represent poorly to well ordered dolomite, respectively (Kaczmarek and Sibley 2011; Pina et al, 2020). Most samples (n=13) are ≥0.60 which is indicative of relatively well ordered dolomite (Kaczmarek and Sibley 2011). Cherty and feldspathic carbonate samples did not exhibit d peaks of (015) or (110) in XRD, and therefore these samples were not included in the stoichiometry and cation ordering averages. Since these analyses are bulk sample measurements, the reported values represent sample averages and are not characteristic of the individual dolomite phases. Stoichiometry for individual dolomite phases was conducted using EPMA spot analyses.

4.2. Microscale textures and mineralogy

4.2.1. Multi-phase dolomite characterization

Composite Red-Green-Blue (RGB) cathodoluminescence maps with R = 450-500 nm, Green = 400-450 nm, and Blue = 350-400 nm reveal three distinct phases of dolomite in all analyzed samples. Dolomite phases vary in crystal size, shape, and intercrystalline boundaries. The three phases of dolomite are classified and characterized by increasing grain size, as microspar, zoned, and saddle, respectively. The microspar (M) dolomite is nonplanar, has closely packed anhedral crystals with irregular, intercrystalline grain boundaries (Fig. 4). The crystals average 20 microns and range 5-40 microns in size. Zoned (Z) dolomite is planar, subhedral to anhedral medium grained (10-100 microns) with straight compromised boundaries. The crystals are concentrically zoned in CL, but not in plane polarized light, and characteristically pore lining or void-filling (Figs 5E, 6). Saddle (S) dolomite is nonplanar, medium (10-100 microns) to coarse grained

(>100 microns) saddle-shaped, void-filling, and exhibits undulatory extinction in cross polarized light (Fig. 7D, E). The three observed CL colors, by increasing wavelength are blue, grey, and gold, and are found throughout the microspar and zoned dolomite phases; the saddle dolomite exhibits a dull bluish color in CL (Fig. 5E). Throughout each phase of dolomite, two CL spectral peaks are present at 389 nm and 650 nm (Fig. 5D).

4.2.2. Porosity types and dissolution features

Open porosity is absent in the studied samples, but occluded pore types of primary and secondary origins were observed. Primary fenestral porosity (≤1 mm in size) is ubiquitous in stromatolite samples and infilled with zoned and saddle dolomite (Fig. 8A, B, C). Vugs are large (2 - 9 mm in average) secondary pores that are at least two times greater in size than the microspar matrix, and are infilled with zoned and saddle dolomite (Fig. 2J). Vugs occur predominately in layers with rip-up clasts and are absent from the lowermost finer grained facies. Secondary microfractures occur in two stages. The first stage includes vertical microfractures (<1 mm wide), infilled with zoned and saddle dolomite, that are present in limited layers of microspar dolomite, and crosscut horizontal laminae and fenestrae in the domal stromatolite (Fig. 8E). The second stage includes randomly oriented microfractures (<1 mm wide) that are present in the oolitic dolosiltite sample B14 and are only infilled with saddle dolomite (Fig. 9).

Dissolution structures of numerous solution seams occur on fresh surfaces as brownish, irregular streaks but appear black on weathered surfaces, and are abundant in the lowermost outcrop layers of finely crystalline, microspar dolomite samples (Fig. 7F). The seams are Fe oxidized-stained but composed of dolomitic material. Microstylolites that parallel the laminae occur throughout sample A3 (Fig. 7G). Stylolites are either dolomitic in composition or, when found along fractured bedding planes, are infilled with quartz, feldspars, and iron oxides.

4.2.3. Thrombolites

The thrombolites exhibit clotted, irregular microtextures (Fig. 7B, C). Rounded microcline and orthoclase, and sub-rounded quartz occur throughout the sample, with small amounts of peloids and ghost grains. SEM/EDS reveals minor mineral components of Fe-oxides and pyrite grains. The detected metal oxide morphologies range from euhedral to highly deformed in shape, and the pyrite has round to sub-round edges (Fig. S2 in supplementary material).

4.2.4. Ooids

The oolitic dolomite layers exhibit nonmimetic replacement (Sibley, 1978) where little or no original texture (radial or tangential) visible except for a dark-colored ooid outline and relics of concentric layers near the nucleus of the ooid (Fig. 10). Ooids vary in size from ~0.25 to 1 mm in diameter.

4.2.5. Stromatolites

The microtexture of the domal stromatolites consists of three distinctly colored layers, as follows: dark grey thinly layered convex-shaped laminae (<1 mm thick), light grey thinly layered convex-shaped laminae (≤1 cm thick) (Fig. 8F, G), and black, very thin (<1 mm) laminae (Fig. 8G). The dark and light grey layers alternate throughout the stromatolites, and the black layers occur predominately in the lower half (Fig. 8G) of the large domal stromatolites. EDS showed no differences in composition between dark and light grey bands of laminae. However, the black laminae are enriched in felsic material (Fig. S3 in supplementary material). Primary fenestral porosity (≤1 mm thick) in the domal stromatolite is parallel to laminae and infilled with zoned and saddle dolomite. Very fine-grained, rounded intraclast rip-ups are situated on the topmost layer (Fig. 8H), which also contains large (<0.5 mm in diameter), rounded feldspars of microcline and orthoclase, and sub-rounded quartz grains. The orthoclase minerals exhibit overgrowth rims (Fig. 8I). The SEM/EDS reveals Ti-oxides, Fe-oxides, pyrite and apatite as minor mineral components (Fig. S2 in supplementary data).

4.3. Geochemistry

4.3.1. Multi-phase dolomite high-resolution elemental analysis

Each phase of dolomite was targeted for microanalyses by electron probe after identification with CL. All three phases of dolomite contain Zn and Mn, and the microspar and zoned dolomite phases have Si (Fig. 5F). The zoned dolomite exhibits dark banding associated with Fe concentrations of 0.4 wt% or higher (Fig. 5G). A compositional trend is observed in the microspar and zoned dolomite phases by a covarying increase in Si with a decrease in Ca and Mg. A decrease in Si abundance and an increase in Fe and Mn abundance is observed across the phases of dolomite (Fig. 5F). No Sr is detected in any phase. The average mol% Ca is 49.3 (n=116 spots analyzed), 49.2 (n=130 spots analyzed), 50.8 (n=131 spots analyzed) for microspar, zoned, and saddle dolomite, respectively. These low Mg- and Ca-excess values translate to Mg/Ca ratio averages of 1.03, 1.03, and 0.97 for microspar, zoned, and saddle dolomite phases, respectively (Table S1 in supplementary material). These values represent stoichiometric microspar and zoned dolomite, and Ca-excess saddle dolomite. The EPMA error for Ca is 0.25% and Mg is 0.47%, so reported values may be closer to stoichiometric than shown.

4.3.2. Carbonate $\delta^{18}O$ and $\delta^{13}C$ composition

Isotope analysis reveals relatively low values of $\delta^{18}O_{dolo}$ (‰ VPDB) and $\delta^{13}C_{dolo}$ (‰ VPDB). Oxygen isotopes ($\delta^{18}O_{dolo}$) range from -18.23‰ to -6.05‰ referenced to VPDB ($1\sigma = 2.79$‰) (Fig. 11, Table S2 in supplementary material). Inorganic carbon isotopes ($\delta^{13}C_{dolo}$) range from -6.54‰ to -0.84‰ referenced to VPDB ($1\sigma = 1.39$‰).

4.3.3. Total organic carbon and organic $\delta^{13}C$ composition

Elemental analysis shows that nitrogen abundance is below detection limits, and organic carbon abundance ranges from is 0.025 to 0.484 wt% (1σ = 0.142 wt%) (Fig. 13, Table S2 in supplementary material). Values of $\delta^{13}C_{org}$ for organic compounds range from -28.25‰ to -25.73‰ referenced to VPDB (1σ = 0.81‰).

4.4. Confocal Raman microscopy

Raman mapping of thin sections reveals that organic carbon, identified by D and G spectral bands, is exclusively associated with the microspar dolomite and commonly situated at or near grain boundaries (Fig. 13). The D and G peaks show slight variations among peak intensity, peak area, and peak position (Fig. 14, Tables S3a and S3b in supplementary material). D and G peak shifts within spectral maps are observed in samples A5 and A16, respectively (Fig. 13C, Fig. S4 in supplementary material). *T*-test results reveal a statistical difference ($p<0.05$) in D band positions, between stromatolite, thrombolite, and oolitic samples (Fig. S5A in supplementary material). The peak shifts in the thrombolite (in D band) and stromatolite (in G band) samples A5 and A16, spatially overlap and occur within the same mapped areas (Figs S5C-E in supplementary material), suggesting there are co-occurrences of different degrees of the organic matter crystallinity within the same analyzed area.

Data quality assessment was done by comparing the computer-fitted cluster method to the more commonly used, manually-fitted Gaussian method. Comparison of the cluster analysis and the Gaussian fitted data shows that the results from the two methods are in overall good agreement with each other, but the Gaussian fit method causes a broader range and relative standard deviation (Table 3). Cluster analysis shows D/G peak intensity ratios average 1.00 ± 0.05; D-FWHM averages 68 ± 34; and D-position averages 1334 ± 12. Gaussian fit analysis shows D/G peak intensity ratios average 1.02 ± 0.75; D-FWHM averages 47 ± 57; and D-position averages 1335 ± 26. All peak parameter results from the cluster and Gaussian fit methods are presented in supplementary material (Table S3a, S3b). In this paper we will focus on the D-band parameters, and the thermometry.

Temperatures derived from Raman geothermometry average 331 ± 73°C, and D band variations show distinct grouping within samples in both peak position (rel cm^{-1}) and FWHM (Fig. 14). The sample grouping corresponds to different temperature ranges: temperatures in average of 368 ± 11°C for oolitic samples; temperature average of 345 ± 43°C for stromatolite samples; and temperature average of 305 ± 12°C for thrombolite samples (Table 4). *T*-test results reveal a statistical difference ($p<0.05$) among the temperature groups of stromatolite and thrombolite (A16 and A5, respectively) and oolitic (A7, B11, B12a) samples, as well as among the thrombolite (A5) and oolitic (A7, B11, B12a) samples (Fig. S6 in supplementary material).

5. DISCUSSION

Characterization of the dolomitization process (including fluid composition and temperature) is fundamentally important when attempting to decipher origin and alteration levels of the organic matter within the host rock. The following sections characterize the depositional environment and the conditions for subsequent dolomitization based on outcrop observations (structural and textural features), petrological (microtextural and cross-cutting relationships), geochemical data, and Raman spectroscopy.

5.1. Sedimentary facies and paleoenvironment

Exposed stratigraphy displays a regression sequence where subtidal high energy ooid shoals transition to intertidal low energy silty lagoonal waters that progress to a supratidal mudcracked tidal flat (Fig. 1C). The dolomitized oolitic grainstone beds were likely ooid shoals that inhibited the incursion of marine waters and formed lower energy lagoon in which overlying finer, silt-sized deposits were formed. On top of the lagoonal deposits are finely laminated domal stromatolites, the beds also include mudcracks, collapse breccias, and tidal channel deposits, all of which is indicative of nearshore, subaerial exposure. The presence of edgewise conglomerate rip-up clasts, jumbled intraclasts, and torn laminae in small stromatolite domes (Fig. 2E) suggest occurrences of high energy storms in nearshore and shallow water. Some layers of lagoonal dolosiltite contain sparse ooids, referred to as oolitic dolosiltite (Table 2). At the top of the outcrop, on the southwest side and adjacent to the large domal stromatolites, are extensive syneresis cracks (Fig. 2N). Syneresis cracks form subaqueously (Plummer and Gostin, 1981), indicating that water levels may have been deeper within the same stratigraphic layer (southwest from the stromatolites). The Allentown Formation’s sedimentological features are consistent with a shallowing peritidal lithological sequence from a transitional marginal-marine setting (Wilson, 1975; Flügel, 2004).

5.1.1. Microtexture and mineralogy

Fine-grained dolomite crystals, finely layered stromatolitic laminae, channel deposits with rip-up clasts, and detrital feldspars and quartz are microtextures formed in tidal flat environment (Siedlecka, 1978; MacNaughton, et al., 2019).

The dark-to-light grey and black stromatolite laminae are characteristic features formed as a result of different mineral assemblages. The data indicate that the black laminae are enriched in silicate minerals, such as detrital quartz and feldspars (Fig. S3 in supplementary materials). The black laminae (<1 mm thick) may have formed during the periods of minor marine flooding when only the smallest particles were carried by low energy waters across the microbial mats (Wilson, 1975). Additionally, scattered siliceous fine grains are found along some dark and light grey stromatolitic laminae, a feature characteristic in regression carbonate evaporitic cycles (Wilson, 1975). Previous Allentown studies (Buie, 1932; Miller, 1941) have attributed the dark-to-light grey color variation to laminae with different concentrations of organic matter and magnesium, stating that beds with high magnesium weather to a lighter color while beds with lower magnesium and more organic content undergo less change in color during weathering. We have not found any evidence of differences in magnesium content within dark-to-light grey layers, and Raman mapping of organics does not show and increased concentration of organic carbon content among dark grey and black laminae compared to light grey laminae.

Accessory minerals pyrite, quartz, and feldspars are most abundant in chert lenses and feldspathic layers. Rounded pyrite and feldspar grains observed in petrological and SEM micrographs indicate their detrital origin. The detritus materials are likely fluvial (Dalton et al., 2014) and aeolian (Miller, 1941) sediments transported by streams and wind. Ti-oxide phases include anatase and rutile, the former being the most abundant, and these minerals are scattered throughout the samples and are not limited to any specific layer(s). Fe-oxides are less common than Ti-oxides and occur sporadically throughout the samples. The distorted Fe- and Ti-oxides observed in this study (Fig. S2 in supplementary material) were likely altered in a different environment before its final deposition and therefore are not indicative of the deposition settings of the study area.

5.2. Dolomitization

The traces of precursory limestone of the Allentown formation have not been identified (Dalton et al., 2014), so the baseline for comparison of dolomitized geochemistry and setting to that of the Cambrian marine setting is missing, which makes interpretations of diagenetic stages or recrystallization settings more difficult. The evidence of the non-stoichiometric metastable magnesium carbonate minerals that are presumed to form during the initial dolomitization stages are missing, indicating that the formation has been entirely replaced by dolomite.

Petrographic features, luminescence, and microprobe analyses suggest multistage dolomitization. Dolomite petrography shows three texturally different crystal phases that are compositionally different (Fig. 5). Determining the order of dolomite crystal formation is essential to reconstruct the paragenetic sequence (Fig. 15) and to reveal if chemical, thermal, or textural overprinting by later crystal generations exists. The following sections discuss the interpreted formation of each phase of dolomite.

5.2.1. Dolomitizing Fluids

The composition of dolomitizing fluids can be constrained by the relative abundance of major and trace elements in dolomite, including the Mg/Ca ratio, Fe, Mn, Zn, Sr, and Si concentrations (Morrow, 1982; Tucker and Wright, 1990; Gasparrini et al., 2006; Zhang et al., 2009; Guido et al., 2018). The Si concentrations detected within the dolomite are not well understood and rarely reported in literature. No detection of Si using Raman spectroscopy suggests Si is not from submicron fluid inclusions or mineral coatings. The EPMA detected Si could be remnant of clay present in the system during dolomitization, a similar mechanism has been proposed for Na (Land, 1980; Kirmaci and Akdag, 2005). Alternatively, Si could have originated from dissolved silica in the seawater (Ramseyer et al., 2013; Dong et al., 2015). The lack of detectable Sr in any of the dolomite phases may be the result of dolomitization in seawater with low Sr content (Vahrenkamp and Swart, 1990), or recrystallization (Land, 1980). Cambrian dolomites formed from seawater can have Sr compositions of <300 ppm (Vahrenkamp and Swart, 1990; Jiang et al., 2019), which is below EPMA detection limits at 0.03 wt%. Therefore, undetectable Sr (<300 ppm) is in line with that expected of dolomites formed from fluids with typical seawater Sr/Ca ratios (Vahrenkamp and Swart, 1990). This, along with the detection of Si, suggests that the Allentown microspar and zoned dolomite phases may have precipitated from seawater (Fig. 5F). Alternatively, it is common in burial diagenesis that Sr and Na concentrations decrease while Fe and Mn increase (Wright and Tucker, 1990; Warren, 2000). The continuous increase in Fe and Mn observed across all dolomite phases when coupled with the presence of saddle dolomite and over burden pressure stylolites indicate an increasing burial origin. The saddle dolomite phase that is enriched in Mn and Fe was likely produced from burial fluids when externally sourced fluids rich in Fe and Mn mixed with the dolomitizing fluids that circulated through the host rock in a water-buffered system (Budd, 1997).

5.2.1.1. Microspar dolomite

Microspar dolomite (M) is a finely crystalline replacive dolomite with microspar-sized crystals (Folk, 1959). An average crystal size of 20 µm was estimated using confocal Raman microscopy. Microcrystalline textures in dolomite (<10 microns) are thought to be from fluids that are highly saturated with respect to dolomite (Sibley, 1991) and are common in early near surface dolomitization (Moore, 1989; Sibley, 1991; Lukoczki et al., 2020; Ryan et al., 2020). This phase of dolomite exhibits nonplanar, irregular intercrystalline grain boundaries (Fig. 4), which is common for crystal growth at temperatures greater than 50°C (Gregg and Sibley, 1984; Sibley and Gregg, 1987; Warren, 2000), however, this texture has also been observed in microspar formed at low temperature, subaerial environments in the presence of concentrated Mg ion solution which enables rapid nucleation of crystals during dolomitization (Sibley and Gregg, 1987; Sijing et al., 2014). The limestone dolomitized early in the marginal marine setting that produced microspar dolomite, the dominant dolomite phase in the studied outcrop (Fig. 4). The preservation of primary porosity (feneastral pores) and fine-scale stromatoltic laminae within microspar beds is evidence for early, near surface dolomitization. Therefore, the microspar dolomite is likely a result of rapid crystal growth under high fluid Mg/Ca ratios.

The CL spectral peaks at 389 nm and 650 nm (Fig. 5D) are due to intrinsic lattice defects in the CO_3^{2-} structure and the substitution of Mg^{2+} with Mn^{2+} into the carbonate lattice, respectively (Walker et al., 1989; Machel et al., 1991; Habermann et al., 1997; Richter et al., 2003). Accordingly, the peak shift that is present at 389 nm (Fig. 5D) may be due to different types of crystallographic lattice defects and if so, variations in crystallographic defects may account for the variations in CL colors of increasing wavelength from blue, grey, to gold (Fig. 5E).

5.2.1.2. Zoned dolomite

Zoned dolomite (Z) occurs as small rhombohedral shaped crystals that infill pore space within the microspar (M) dolomite (Fig. 6A), and larger cavity lining crystals that exhibit patchy rhombic cores in CL but not in plane polarized light (Fig. 6B). The rhombohedral cores are chemically distinct from the zonation bands that outline them. The cores exhibit the same blue, grey, gold CL characteristics as the microspar and may represent penecontemporaneous formation with the microspar dolomite, from the same type of fluids. Additionally, microspar and zoned dolomite contain trace amounts of Si (Fig. 5F) which also suggest the same formational fluids for both phases. The presence of patchy cores detected in CL, but not PPL, within some of the larger rhombic cores is not well understood. Some studies suggest this pattern is derived from inhomogenous fluids during growth (Kaczmarek and Sibley 2014), multiple dolomite dissolution-precipitation phases (Sena et al., 2014), or inclusions (Budd, 1997). We do not see evidence for inhomogeneous fluids from EPMA line scans, and Raman did not detect any non-carbonate related peaks to explain inclusions. We also do not have additional evidence for dissolution preci

The concentric pattern of zonation, that outlines the rhombic cores, is a result of primary crystal growth stages and relates to the fluctuating fluid chemistry during formation (Reeder, 1991; Budd 1997). The crystal zones altered between Ca:Mg zones (light bands) and Fe:Mg zones (dark bands) indicating changes in Ca, Mg and Fe concentrations in dolomitizing fluids during the crystal growth (Fig. 5G, 6B). The dark bands are likely from Fe- and Mn-rich fluids that periodically entered the system during dolomitization.

5.2.1.3. Saddle dolomite

Ongoing, deeper burial produced late stage chemical compaction from overburden pressure resulting in stylolites, and localized dissolution seams that are concentrated in the lagoonal facies and occur throughout the outcrop. The second stage of microfracturing produced fractures that later infilled with saddle dolomite. The dull luminescence of saddle dolomite (S), Fe-rich chemistry, and saddle shape are all features of late stage, high temperature dolomite formation (Machel, 1987; Radke and Mathis, 1980; Warren, 2000). Although there is no direct evidence for primary precipitation, the lack of floating particles of other minerals within the crystals, and the lack of irregular and sutured crystal boundaries, indicate that this is not a replacement phase (Radke and Mathis, 1980), but rather a primary precipitate during burial diagenesis. Possible penecontemporaneous formation of saddle dolomite and stylolites may be inferred from one crosscutting feature observed at the outcrop, where an overlying stylolite seemed collapsed into a large vug and is surrounded by the infilling saddle dolomite (Fig. 2Q). The saddle dolomite was likely formed in a water-buffered, isotopically open, system where Fe and Mn fluids were incorporated into the dolomite along with the Mg/Ca dolomitizing fluids (Budd, 1997). This final stage of burial diagenesis, thermally overprinted the entire formation as revealed from organic carbon Raman D and G bands and previous CAI thermometry temperatures of the microspar dolomite (Table 4).

Based on petrographic features, CL, and EPMA, the three dolomite crystal phases are multi-generational and formed over three stages (Fig. 15) The first, second, and third generations of dolomite are microspar, zoned, and saddle, respectively.

5.2.2. Carbonate $\delta^{18}O$ and $\delta^{13}C$ composition

The low $\delta^{18}O_{dolo}$ values (-18.23‰ to -6.05‰ VPDB) reflect the deep burial diagenetic setting where the saddle dolomite formed (Haas et al., 2017; Al-Aasm and Crowe, 2018), in an isotopically open system and at higher temperatures than those of microspar and zoned dolomite formation. This burial signature may not be the only influence on $\delta^{18}O_{dolo}$ values, but there are no apparent correlations to depth or sample facies, and therefore a further interpretation is not attainable at the moment.

A comparison of $\delta^{18}O_{dolo}$ values from the micro-drilled saddle and microspar shows that these values cannot be differentiated from bulk carbonate $\delta^{18}O_{dolo}$ values as they fall within the range of error bars (Fig. 11). An isotopically open system, or the resetting of isotopes during burial diagenesis or recrystallization under high temperatures (Land, 1980; Malone et. al., 1994; Warren, 2000; Swart, 2015) could explain the overlap of $\delta^{18}O_{dolo}$ values in dolomite phases (Fig. 11). Because burial diagenesis and recrystallization can result in the same signatures (Kaczmarek and Sibley, 2014), the Allentown dolomite, if recrystallized, would be significantly recrystallized with respect to depleted $\delta^{18}O$, and insignificantly recrystallized with respect to all other evaluated parameters (Machel, 1997). However, due to burial evidence (e.g., stylolites) the depleted $\delta^{18}O$ signature is likely more appropriately attributed to a burial diagenetic setting.

Variations in the origin of sedimentary materials and diagenesis should be taken into account when interpreting the $\delta^{13}C_{dolo}$ and $\delta^{13}C_{org}$ (Swart, 2015). The low $\delta^{13}C_{dolo}$ values (e.g., -6‰ VPDB) can indicate thoroughly altered isotopic compositions, as a result of diagenesis in an open system with high fluid:rock ratios (Lohmann, 1988; Sharp, 2007). This interpretation corresponds well with findings of the saddle dolomite in the Allentown samples. In order for saddle dolomite to form, the Fe and Mn-rich fluids needed to mix with the dolomitizing (Mg/Ca) fluids which requires a high fluid:rock ratio most likely found in an open system (Brand and Veizer, 1980; Budd, 1997). This interpretation fits well with the Allentown $\delta^{13}C_{dolo}$ values (Fig. 11) and petrographic data. Alternatively, the low $\delta^{13}C_{dolo}$ values may derive from diagenetic alteration of oxidized organics in the system (Irwin et al., 1977; Lohmann, 1988; Schidlowski, 1988; Lamb et al., 2006; Swart, 2015). The relatively low TOC (Table S2 in supplementary material) in the Allentown samples suggests that the organic signature is not likely the main, or single, influence on $\delta^{13}C_{dolo}$ values.

Coupling of $\delta^{18}O_{dolo}$ and $\delta^{13}C_{dolo}$ isotopes suggests contemporaneous alteration from the same source(s) for both $\delta^{18}O_{dolo}$ and $\delta^{13}C_{dolo}$ isotopes and all samples (Fig. 12B) (Des Marais et al., 1992; Jiang et al., 2012). The decoupled trends of $\delta^{13}C_{org}$ with $\delta^{18}O_{dolo}$ and $\delta^{13}C_{dolo}$ may be related to diagenetic alteration in a system that was not rock buffered and does not retain the original $\delta^{13}C_{dolo}$ values (Grotzinger et al., 2011; Jiang et al., 2012; Oehlert and Swart, 2014). The decoupling trend may occur due to variations in $\delta^{13}C_{org}$ values that may reflect mixed organic sources and diagenesis (Swart, 2015). Alternatively, the decoupled $\delta^{13}C_{org}$ and $\delta^{13}C_{dolo}$ values may imply relatively unaltered values that reflect values of the shallow water organic matter. In this scenario a lack of correlation between the two values may occur due to the wide range of

$\delta^{13}C$ values from organic matter and a relatively narrow range in $\delta^{13}C$ values from inorganic matter (Oehlert et al., 2012; Swart, 2015).

Jiang et al. (2012) reported decoupled $\delta^{13}C_{org}$ and $\delta^{13}C_{dolo}$ in Cambrian carbonates with low TOC (<0.1 wt %) and interpreted this as a result of diagenetic alteration of organic carbon and/or amplification of detrital organic carbon isotope signature in organic-poor carbonates. In an oxidizing setting, primary marine-derived organic carbon will degrade faster than terrestrial organics, and a low TOC (<0.2 wt %) and negative $\delta^{13}C_{org}$ can result (Oehlert and Swart, 2014). Evidence for various organic matter sources is supported by Raman data where D and G bands cluster based on the type of carbonate deposit (stromatolite, thrombolite, and oolitic) in tidal flat to shoal facies). Additionally, Lamb et al. (2006) showed that the provenance of organic matter sources is environment-depended and vary within the peritidal sequence of a coastal environment.

Based on the Allentown's depleted isotope measurements, low TOC, high temperature and burial settings (saddle dolomite, stylolites), diagenesis effects cannot be excluded and the decoupled isotopic values likely resulted from diagenetic alteration of organic carbon and/or amplification of detrital organic carbon isotope signature in these organic-poor carbonates (Jiang et al., 2012).

5.3. Characterization of organic carbon

Organic carbon is characterized based on TOC, $\delta^{13}C_{org}$, Confocal Raman microscopy, and D and G peak analyses in order to determine spatial relationships between organic matter and minerals, alteration and thermal maturity of the organic carbon.

5.3.1. TOC and $\delta^{13}C_{org}$

The samples with higher TOC concentrations (0.484 to 0.286 wt%) have lighter $\delta^{13}C_{org}$ compositions (-28.25 to -27.45‰ relative to VPDB), while samples with lower TOC (0.025 to 0.120 wt%) show heavier $\delta^{13}C_{org}$ compositions (-27.44 to -25.73‰ relative to VPDB**)** (Fig. 12A). Such a decrease in TOC coupled with heavier $\delta^{13}C_{org}$ values may be indicative of post-depositional thermal degradation (McKirdy and Powell, 1974; Strauss and Beukes, 1996; Eigenbrode and Freeman, 2006; Jiang et al., 2012).

Oolitic dolosiltite sample B9 has the highest TOC at 0.48 wt%; this sample contains rip-up clasts, which are characteristic for tidal channel deposits formed during storms. The increase in TOC within samples B9, and oolitic dolarenite samples B10, B11, and oolitic dolosiltite sample B13, all of which include evidence of high energy, storm events (rip-up clasts and edgewise conglomerates), which had capacity to deliver additional organic input within these layers.

The input of terrestrial organic matter washed in during storms in supra- to inter-tidal areas could had been incorporated in the sediments and stromatolitic laminae and in the thrombolites during deposition and contributed to the mixed pools signatures as seen in Raman (Fig. 13B) and $\delta^{13}C_{org}$ (Table S2 in supplementary material).

The measured values of $\delta^{13}C_{org}$ range from -25.73‰ to -28.25‰ relative to VPDB (Fig. 12B), which is broadly consistent with organic input from decaying organic matter or microbial metabolism (Irwin et al., 1977; Schidlowski, 1988; Lamb et al., 2006). The lighter values of oolitic samples (B transect) from the subtidal area likely reflect marine organics (Lamb et al., 2006), while the stromatolites and thrombolites include a mixture of terrestrial and marine organics and therefore exhibit a bit heavier values (see Fig. 12A) (Lamb et al., 2006).

5.3.2. Characterization of organic carbon based on confocal Raman spectroscopy

The spatial relation of the organic carbon to multi-generational dolomite is significant for determining if the carbon was already in place before dolomitization, and therefore syngenetic with the Cambrian stromatolites. Confocal Raman microscopy reveals that D and G bands of organic carbon are only present in the first generation of microspar dolomite and situated at or near grain boundaries.

5.3.2.1. Raman thermometry

A commonly used geothermometer method is oxygen isotope ratios to estimate the thermal history of carbonate minerals (Friedman and O’Neil, 1977; Land, 1983). The measured oxygen isotope values in this study reflect the late burial fluids from an open system that has replaced the Cambrian isotopic seawater values and rendered them unusable (Land, 1980; Sharp, 2007).

The color alteration index (CAI) of conodont fossils is another method used as a geothermometer for sedimentary rocks (Epstein et al., 1977; Marshall et al., 2001). Conodont fossils found in Warren and Sussex counties of New Jersey Allentown outcrops have CAI (Epstein et al., 1977; Helsen et al., 1995) values of 5 indicating temperatures of at least 300°C and burial depths of at least 10 km (Harris et al., 1995). Burial depths around 10 km would correspond to burial pressure of at least 300 MPa (Tilley, 1924). Based on our outcrop observations and microtextural evidence, this outcrop had not been exposed to unidirectional stress that would align or elongate grains, but the pressure was likely lithostatic and uniform pressure derived from the burial process.

Organic carbon first-order bands of Raman spectra (D and G bands at ~1350 and 1600 cm^{-1}, respectively) record the host rock’s maximum temperature and can be used as an organic paleothermometer (Pasteris and Wopenka, 1991; Wopenka and Pasteris, 1993; Marshall et al., 2001; Marshall et al., 2012). The G band is the ordered, graphitic structure of carbon, and the D band is the disordered carbon structure. Variations in the bands, related to differing amounts of thermally induced rearrangement, can be used to determine structural order of the carbon and associated temperature setting required for such level of crystallinity (Pasteris and Wopeneka, 1991; Beyssac et al., 2002). Calculated temperatures yield a range of 300 - 373°C (±30°C) for the Allentown organic carbon. This type of organic carbon alteration is also reflected in the overall D and G band spectral characteristics, which exhibit D3 and D4 bands, and commonly have D and G bands that are equal in intensity (Table 3, Tables S3a, S3b in supplementary material). These newly calculated temperatures based on Raman data corroborate previously estimated temperatures based on conodont fossil CAI values.

Within the newly derived temperatures, three distinct groups of organic carbon differentiate (Fig. 14) stromatolite (A16), thrombolite (A5), and oolitic samples (A7, B11, B12a). The D band positions and associated temperatures are statistically different ($p<0.05$) between these rock types (Fig. S5 in supplementary material). Variations in D band characteristics may be related to different starting organic matter (e.g., marine vs terrestrial), because the temperatures do not correlate with strata depth. For example, thrombolites record the lowest temperatures, while the stromatolites, which are coeval to or younger than thrombolites (Figs 1C, 3), have higher average temperatures. The clear interpretation of these groups is not attainable at the moment; however, based on the fact that they are separated as different facies, we may assume that different types of starting organic material contained in different facies may had altered differently despite the same diagenetic setting (Wopenka and Pasteris, 1993).

5.4. Organic carbon origins

Based on the spatial distribution and exclusive occurrence of organic material in the replacive microspar dolomite, it is very possible that the organic carbon was trapped in the samples during the original limestone lithification and already in place during the dolomitization (Fig. 13A, Figs S5C-E in supplementary material). This early dolomitization likely occurred from seawater supersaturated in Mg ions, that rapidly produced stoichiometric dolomite, a thermodynamically stable phase (Carpenter, 1980; Nordeng and Sibley, 1994; Mueller et al., 2019), which resisted further alteration during burial diagenesis and preserved the Cambrian organics. The placement of organic carbon suggests it is indigenous and syngenetic to the primary fabric of the host rock. The Raman cluster maps show the peak variations overlap spatially (Fig. 13B and Figs S5C-E in in supplementary material), suggesting all three varieties of organics were in place at the same time, matching the alteration temperature of the host rock.

Claims of biogenicity of organic carbon that is not associated with cellular morphological evidence should be approached with caution. The finding of organic carbon with an isotopic composition that may be indicative of microbial metabolism is not an explicit line of evidence for biogenicity (Braiser et al., 2004; De Gregorio and Sharp, 2006). Organic molecules can form from abiotic, autochthonous chemical reactions such as Fischer-Tropsch type processes in hydrothermal environments and decarbonation during metamorphism (McCollom and Seewald, 2006; Galvez et al., 2013; Bernard and Papineau, 2014). Although this null hypothesis cannot be fully rejected, there is no evidence of such hydrothermal processes in the outcropping area.

The evidence for Allentown organic carbon that is likely of biogenic origin are: 1) organic carbon is exclusive to the primary fabric (microspar dolomite) of the host rock which indicates a syngenetic origin, 2) the geological context is a marginal-marine setting that is a favorable habitat to marine organisms and overall rich in biological organic material, and one of the obvious sources of organics are numerous microbial stromatolite macrostructures observed at the ourcrop, and 3) geochemical signals of $\delta^{13}C_{org}$ values are indicative of biology and consistent with decaying organic matter or microbial metabolism (Irwin et al., 1977; Schidlowski, 1988; Lamb et al., 2006). Although the detection of disordered carbon by Raman spectroscopy is not alone indicative of biogenicity (Pasteris and Wopenka, 2003), the variations within D and G bands may be indicative of various alteration levels due to different types of starting material.

The degree of crystallinity in carbonaceous matter is affected by the type of organic matter and host rock composition during heating (Wopenka and Pasteris, 1993), therefore, the D and G peak differences may be due to different types of organic starting material that altered, or decomposed, differently despite the same alteration setting (Lamb et al., 2006). The peak shifts in D and G band positions within the same mapped area (e.g., Fig. 13) is indicative of three different phases of organic carbon, which suggests different source pools of indigenous and syngenetic organic material. Lamb et al. (2006) reported organic matter in Holocene lagoonal and tidal flat sediments is mostly derived from suspended particulate organic matter such as plant detritus and phytoplankton from river and marine sources, respectively. This variation in tidal flat organics may potentially explain how three phases of organic carbon are found in the the stromatolite and thrombolite samples (A16 and A5, respectively), while oolitic (A7, B11 and B12a) samples only have one carbon phase present (Fig. 13, Fig. S4a in supplementary material). Since no nitrogen was detected by IRMS, characterization of organic sources based on C/N ratios (e.g., Lamb et al., 2006) is not possible. Instead, using the $\delta^{13}C_{org}$ values alone show an overlap of marine and freshwater organic carbon (Lamb et al., 2006).

6. CONCLUSIONS

Traditionally, secondary, stoichiometric, and ordered dolomite has been hypothesized to occur at either high temperatures or from multiple stages of recrystallization (Machel, 1978;

Kupecz et al., 1993; Gregg et al., 2015) that would likely erase evidence of original texture, chemistry, and biology (Gregg and Sibley, 1984; Grotzinger and Knoll, 1999; Schopf, 1999; Warren, 2000). The results presented here indicate that stoichiometric and ordered dolomite can form within early dolomitization settings, undergo increasing temperature and burial diagenesis, and still retain syngenetic organic carbon. In summary:

- Outcrop scale observations (mudcracks, collapse breccia, rip-up clasts and edgewise conglomerates) and petrological microtextures characteristics (finely-laminated stromatolites, fenestral porosity, rip-up clasts, finely crystalline microspar dolomite) reveal that the Allentown depositional setting was a tidal flat along the Cambrian coastline where original calcium carbonate mineral precursors dolomitized early in a marginal marine setting.
- Bulk dolomite varies in cationic ordering from poorly to well ordered, and the stoichiometry varies from low Ca-excess to stoichiometric to low Mg-excess. Individual phases of dolomite are stoichiometric (microspar and zoned) and Ca-enriched (saddle).
- Geochemical characteristics recorded by each phase of dolomite suggests two dolomitization processes dominated, early dolomitization in the marginal marine setting and late dolomitization from deep burial diagenesis.
- Microspar and zoned dolomite phases formed by dolomitization in high Mg/Ca fluids, the evidence for which are found in the presence of finely crystalline replacive dolomite crystals, and the preservation of primary depositional features such as fenestral porosity. Saddle dolomite formed by burial dolomitization as revealed by coarse void-filling crystals, dull luminescence, Fe and Mn enrichment, and low $\delta^{18}O_{dolo}$ values.
- Burial diagenesis likely thermally overprinted the microspar and zoned dolomite, as revealed by Raman thermometry.

- Raman D and G bands indicate greenschist-like thermal maturity of organic carbon within the formation which is in agreement with conodont fossil CAI geothermometry previously reported for the Allentown dolostone.
- Organic carbon is found at or near grain boundaries, exclusively within the first generation of microspar dolomite. This suggests the organics were in place when the grains of dolomite formed, indicating indigenous and syngenetic origin of the organic carbon within the Cambrian stromatolites.
- Identification by Raman spectroscopy of various pools of organic carbon were found in stromatolite, thrombolite, and oolitic deposits indicating that indigenous and syngenetic organic matter can be identified in many dolomitized facies.

6.1. Astrobiological relevance

This work shows that biosignature (e.g., organic carbon) preservation in carbonate environments extends beyond obvious microbial structures (e.g. stromatolites and thrombolites) and may also be preserved in shallow water environments that were rich in microbial life (e.g., coastal, marginal marine environments). This type of research is especially important when searching for life on other planets because microbial fossil preservation on Earth is rare, and different geologic environments and evolutionary histories on other planetary bodies will likely result in different types of life signatures recorded in the rocks. Terrestrial analogs such as this study will allow for better interpretations of potential biosignatures in Martian carbonates, which may have undergone varying levels of alteration. Based on the data presented in this paper, the textural and mineralogical evidence that may be indicative of life and biosignature preservation in carbonate environments is not limited to silicified carbonates or obvious microbial structures (stromatolites), but extends to dolomitized carbonates and general shallow water settings, where fine-grained carbonate minerals indicate primary environments that are capable of preserving indigenous and syngenetic organic carbon. The Mars Perseverance rover has the ability to target fine-grained carbonate rock, such as the microspar dolomite in this study, for Raman analysis, and if carbon is detected, these may serve as high potential biosignatures to be cached for future sample return mission(s).

ACKNOWLEDGMENTS

We are grateful to Alexander Gates and Michael Kalczynski for their assistance with field trip logistics and sample collection. This study was funded by NASA ASTEP (NNX14AT28G to M.G.) and NASA NAI ENIGMA – Rutgers University (80NSSC18M0093).

DATA AVAILABILITY

Supplementary data related to this article can be found at http://dx.doi.org/10.17632/k57gbw78d9.3, hosted at Mendeley Data (Murphy et al., subm).

REFERENCES

Al-Aasm, I.S., Crowe, R., 2018. Fluid compartmentalization and dolomitization in the Cambrian and Ordovician successions of the Huron Domain, Michigan Basin. Mar. Petrol. Geol. 92, 160-178.

Allan, J.R., Wiggins, W.D., 1993. Dolomite reservoirs: geochemical techniques for evaluating origin and distribution, AAPG Continuing Education Course Notes No. 36. American Association of Petroleum Geologists, Tulsa, OK. 129 pp.

Allwood, A.C., Walter, M.R., Kamber, B.S., Marshall, C.P., Burch, I.W., 2006. Stromatolite reef from the Early Archaean era of Australia. Nature 441, 714-718.

Ayllón-Quevedo, F., Souza-Egipsy, V., Sanz-Montero, M.E., Rodríquez-Aranda, J.P., 2007. Fluid inclusion analysis of twinned selenite gypsum beds from the Miocene of the Madrid basin (Spain). Implication on dolomite bioformation. Sed. Geol. 201, 212-230.

Barghoorn, E.S. Tyler, S.A., 1965. Microorganisms from the Gunflint Chert: These structurally preserved Precambrian fossils from Ontario are the most ancient organisms known. Science 147, 563-75.

Bartley, J.K., Knoll, A.H., Grotzinger, J.P., Sergeev, V.N., 2000. Lithification and fabric genesis in precipitated stromatolites and associated peritidal carbonates, Mesoproterozoic Billyakh Group, Siberia. In: Grotzinger, J. P., James, M. P. (Eds.), Carbonate Sedimentation and Diagenesis in the Evolving Precambrian World. SEPM Spec. Publ. 67, pp. 59-73.

Bernard, S. Papineau, D., 2014. Graphitic Carbons and Biosignatures. Elements 10, 435-440.

Beyssac, O., Goffe, B., Chopin, C., Rouzaud, J. N. 2002. Raman spectra of carbonaceous material in metasediments: a new geothermometer. J. Metamorphic Geol. 20, 859-871.

Blakey, R., 2016. Global Paleogeography and Tectonics in Deep Time Series. Colorado Plateau Geosystems Inc. https://deeptimemaps.com/wp-content/uploads/2016/05/500_ma_Cambrian_GPT-1.png (Accessed 6 July 2020).

Bragg, W.H. Bragg W.L., 1913. The Reflection of X-rays by Crystals. Proceedings of the Royal Society of London. Series A, Containing Papers of a Mathematical and Physical Character 88, 428-438.

Braiser, M., Green, O., Lindsay, J., Steele, A., 2004. Earth's oldest (~3.5 Ga) Fossils and the 'Early Eden Hypothesis': Questioning the Evidence. Origins Life Evol. Biosph. 34, 257-269.

Braiser, M.D., Antcliffe, J., Saunders, M., Wacey, D., 2015. Changing the picture of Earth's earliest fossils (3.5–1.9 Ga) with new approaches and new discoveries. PNAS 112, 4859.

Brand, U., Veizer, J., 1980. Chemical Diagenesis of a Multicomponent Carbonate System – 1: Trace Elements. J. Sediment. Petrol. 50, 1219-1236.

Budd, D.A., 1997. Cenozoic dolomites of carbonate islands: their attributes and origin. Earth-Science Reviews. 42, 1-47.

Buick, R. 1990. Microfossil Recognition in Archean Rocks: An Appraisal of Spheroids and Filaments from a 3500 M.Y. Old Chert-Barite Unit at North Pole, Western Australia. Palaios 5, 441-459.

Buie, B.F., 1932. A Report of Investigations of the Allentown Limestone Formation. Unpublished Master's Thesis. LeHigh University, PA.

Cady, S.L., Farmer, J.D., Grotzinger, J.P., Schopf, J.W., Steele, A., 2003. Morphological Biosignaures and the Search for Life on Mars. Astrobiology. 3, 351-368.

Carpenter, A.B., 1980. The chemistry of dolomite formation I: the stability of dolomite. In: Zenger, D.H., Dunham, J.B., Ethington, R.L. (Eds.), Concepts and Models of Dolomitization. Spec. Publ. Soc. Econ. Paleont. Miner. 28, 11-122.

Calça, C.P., Fairchild, T.R., Cavalazzi, B., Hachiro, J., Petri, S., Huila, M.F.G., Toma, H.E., Araki, K., 2016. Dolomitized cells within chert of the Permian Assistência Formation, Paraná Basin, Brazil. Sediment. Geol. 335, 120-135.

Dalton, R.F., Volkert, R.A., Monteverde, D.H., Herman, G.C., Canace, R.J., 2014. Bedrock Geologic Map of the Hamburg Quadrangle, Sussex County, New Jersey (1:24,000). New Jersey Geological and Water Survey, Trenton, NJ.

De Gregorio, B.T. Sharp, T.G., 2006. The structure and distribution of carbon in 3.5 Ga Apex chert: Implications for the biogenicity of Earth's oldest putative microfossils. Amer. Miner. 91, 784-789.

D'Elia, M., Blanco, A., Galiano, A., Orofino, V., Fonti, S., Mancarella, F., Guido, A., Russo, F., Mastandrea, A., 2017. SEM morphological studies of carbonates and the search for ancient life on Mars. Int. J. Astrobiology. 16, 137-142.

Des Marais, D.J., Strauss, H., Summons, R.E., Hayes, J.M., 1992. Carbon isotope evidence for the stepwise oxidation of the Proterozoic environment. Nature 359, 605-609.

Dong, L. Shen, B., Lee, C.A., Shu, X., Peng, Y., Sun, Y., Tang, Z., Rong, H., Lang, X., Ma, H., Yang, F., Guo, W., 2015. Germanium/silicon of the Ediacaran-Cambrian Laobao cherts: Implications for the bedded chert formation and paleoenvironment interpretations. Geochem. Geophys. Geosyst. 16, 751-763.

Drake Jr., A.A., 1965. Carbonate Rocks of Cambrian and Ordovician Age Northampton and Bucks Counties, Eastern Pennsylvania and Warren and Hunterdon Counties, Western New Jersey. Bull. US Geol. Surv. 1194-L. 12 pp.

Eigenbrode, J.L. Freeman, K.H., 2006. Late Archean rise of aerobic microbial ecosystems. PNAS 103, 15759-15764.

Epstein, A.G., Epstein, J.B., Harris, L.D., 1977. Conodont Color Alteration – an Index to Organic Metamorphism. US Geol. Surv. Professional Paper 995.

Flügel, E., 2004. Carbonate Depositional Environments. In: Flügel, E. (Ed.), Microfacies of Carbonate Rocks. Springer, Berlin, Heidelberg. pp. 7-52.

Folk, R.L., 1959. Practical petrographic classification of limestones. Bull. Amer. Assoc. Petrol. Geol. 43, 1-38.

Friedman, I. O'Neil, J.R., 1977. Compilation of stable isotope fractionation factors of geochemical interest. US Geol. Surv. Professional Paper 440-KK. 11 pp.

Galvez, M.E., Beyssac, O., Martinez, I., Benzerara, K., Chaduteau, C., Malvoisin, B., Malavieille, J., 2013. Graphite formation by carbonate reduction during subduction. Nature Geoscience 6, 473-477.

Gasparrini, M., Bechstädt, T. Boni, M., 2006. Massive hydrothermal dolomites in the southwestern Cantabrian Zone (Spain) and their relation to the Late Variscan evolution. Mar. Petrol. Geol. 23, 543–568.

Goldsmith, J.R., Graf, D.L., 1958. Relation between lattice constants and composition of the Ca-Mg carbonate. Am. Mineral. 43, 84-101.

Graf, D.L., Goldsmith, J.R., 1956. Some Hydrothermal Syntheses of Dolomite and Protodolomite. J. Geol. 64, 173-186.

Gregg, J.M., Bish, D.L., Kaczmarek, S.E., Machel, H.G., 2015. Mineralogy, nucleation and growth of dolomite in the laboratory and sedimentary environment: A review. Sedimentology 62, 1749-1769.

Gregg, J.M., Sibley, D.F., 1984. Epigenetic dolomitization and the origin of xenotopic dolomite texture. J. Sediment. Petrol. 54, 908-931.

Grotzinger, J.P., Rothman, D.H., 1996. An abiotic model for stromatolite morphogenesis. Nature 383, 423-425.

Grotzinger, J.P., Knoll, A.H., 1999. Stromatolites in Precambrian Carbonates: Evolutionary Mileposts or Environmental Dipsticks? Annu. Rev. Earth Planet. Sci. 27, 313-358.

Grotzinger, J.P., Fike, D.A., Fischer, W.W., 2011. Enigmatic origin of the largest-known carbon isotope excursion in Earth’s history. Nat. Geosci. 4, 285-292.

Guido, A., Russo, F., Miriello, D., Mastandrea, A., 2018. Autochthonous Micrite to Aphanodolomite: The Microbialites in the Dolomitization Process, Geosciences 8, 451. https://doi.org/10.3390/geosciences8120451.

Haas, J., Hips, K., Bundai, T., Gyori, O., Lukoczki, G., Kele, S., Demeny, A., Poros, Z., 2017. Processes and controlling factors of polygenetic dolomite formation in the Transdanubian Range, Hungary: a synopsis. Int. J. Earth Sci. 106, 991-1021.

Habermann, D., Götze, J., Neuser, R., Richter, D.K., 1997. The phenomenon of intrinsic cathodoluminescence: Case studies of quartz, calcite and apatite. Zentralbl Geol Paläont Teil 1, Heft 10–12, 1275–1284.

Harris, A.G., Repetski, J.E., Stamm, N.R., Weary, D.J., 1995. Conodont Age and CAI Data for New Jersey. US Geol. Surv. Open-File Report 95-557. 32 pp.

Helsen, S., David, P., Fermont, W.J.J., 1995. Calibration of Conodont Color Alteration Using Color Image Analysis. J. Geol. 103, 257-267.

Hips, K., Haas, J., Poros, Z., Kele, S., Budai, T., 2015. Dolomitization of Triassic microbial mat deposits (Hungary): Origin of microcrystalline dolomite. Sed. Geol. 318, 113-129.

Hoffman, H.J., 2013. Archean Stromatolites as Microbial Archives. In: Microbial Sediments, R.E. Riding, S.M. Awramik, (Eds.), Springer, Springer Berlin Heidelberg, 315-327.

Horgan, B.H.N., Anderson, R.B., Dromart, G., Amador, E.S., Rice, M.S., 2020. The mineral diversity of Jezero crater: Evidence for possible lacustrine carbonates on Mars. Icarus 339, 113526. https://doi.org/10.1016/j.icarus.2019.113526.

Howell, B.F., 1945. Revision of Upper Cambrian faunas of New Jersey, Geological Society of America, Memoir 12. pp. 1355-1368.

Irwin, H., Curtis, C., Coleman, M., 1977. Isotopic evidence for source of diagenetic carbonates formed during burial of organic-rich sediments. Nature, 269, 209-213.

Jiang, G., Wang, X., Shi, X., Xiao, S., Zhange, S., Dong, J., 2012. The origin of decoupled carbonate and organic carbon isotope signatures in the early Cambrian (ca. 542-520 Ma) Yangtze platform. Earth Planet Sci Lett. 317-318, 96-110.

Jiang, W., Hou, M., Wang, C., 2019. Strontium isotopic compositions of Cambrian (Upper Miaolingian–Furongian Series) dolomites from south-eastern Sichuan Basin, China: Significance of sources of dolomitizing fluids and timing of dolomitization. Mar. and Petrol. Geol. 109, 408-418.

Kaczmarek, S.E., Sibley, D.F. 2011., On the evolution of dolomite stoichiometry and cation order during high-temperature synthesis experiments: An alternative model for the geochemical evolution of natural dolomites. Sed. Geol. 240, 30-40.

Kaczmarek, S.E., Sibley, D.F., 2014. Direct physical evidence of dolomite recrystallization. Sedimentology 61, 1862-1882.

Kirmaci, M.Z., Akdag, K., 2005. Origin of dolomite in the Late Cretaceous-Paleocene limestone turbidites, eastern Pontides, Turkey. Sed. Geol. 181, 39-57.

Knoll, A.H. Strother, P.K., Rossi, S., 1988. Distribution and Diagenesis of Microfossils from the Lower Proterozoic Duck Creek Dolomite, Western Australia. Precambr. Res. 38, 257-279.

Kouketsu, Y., Mizukami, T., Mori, H., Endo, S., Aoya, M., Hara, H., Nakamura, D., Wallis, S., 2014. A new approach to develop the Raman carbonaceous material geothermometer for low-grade metamorphism using peak width. Island Arc 23, 33-50.

Kupecz J.A., Montanez I.P., Gao, G., 1993. Recrystallization of Dolomite with Time. In: Rezak, R., Lavoie, D.L. (Eds.), Carbonate Microfabrics. Frontiers in Sedimentary Geology. Springer, New York, NY. pp 187-193.

Lamb, A.L., Wilson, G.P., Leng, M.J., 2006. A review of coastal palaeoclimate and relative sea-level reconstructions using $\delta^{13}C$ and C/N ratios in organic material. Earth Sci. Rev. 75, 29-57.

Land, L.S., 1980. The isotopic and trace element geochemistry of dolomite: The state of the art. In: Zenger, D.H., Dunham, J.B., Ethington, R.L. (Eds.), Concepts and Models of Dolomitization. SEPM Spec. Publ. 28, pp. 87-110.

Land, L. S., 1983. The Application of Stable Isotopes to Studies of the Origin of Dolomite and to Problems of Diagenesis of Clastic Sediments. In: Arthur, M. A. (Ed.) Stable Isotopes in Sedimentary Geology. SEPM Short Course No. 10, pp.1-22.

Lindtke, J., Ziegenbalg, S.B., Brunner, B., Rouchy, J.M., Pierre, C., Peckmann, J., 2011. Authigenesis of native sulphur and dolomite in a lacustrine evaporitic setting (Hellín basin, Late Miocene, SE Spain). Geol. Mag. 148, 655-669.

Lohmann, K.C., 1988. Geochemical patterns of meteoric diagenetic systems and their application to studies of paleokarst. In: James, N. P., Choquette, P. W. (Eds.), Paleokarst. Springer-Verlag, New York, pp. 58–80.

Lukoczki, G., Haas, J., Gregg, J.M., Machel, H.G., Kele, S., John, C.M., 2020. Early dolomitization and partial burial recrystallization: a case study of Middle Triassic peritidal dolomites in the Villany Hills (SW Hungary) using petrography, carbon, oxygen, strontium and clumped isotope data. Int. J. Earth Sci. 109, 1051-1070.

Lumsden, D.N., 1979. Discrepancy between thin-section and X-ray estimates of dolomite in limestone. J. Sed. Petrol. 49, 429-436.

Machel, H.G., 1978. Dolomites and dolomitization. In: Sedimentology. Encyclopedia of Earth Science. Springer, Berlin, Heidelberg. doi: 10.1007/3-540-31079-7.

Machel, H.G., 1987. Saddle dolomite as a by-product of chemical compaction and thermochemical sulfate reduction. Geology 15, 936-940.

Machel, H.G., 1997. Recrystallization versus neomorphism, and the concept of 'significant recrystallization' in dolomite research. Sed. Geol. 113, 161-168.

Machel, H.G., 2004. Concepts and models of dolomitization – a critical reappraisal. In: Braithwaite, C.J.R., Rizzi, G., Darke, G. (Eds.), The Geometry and Petrogenesis of Dolomite Hydrocarbon Reservoirs. Geol. Soc. London, Spec. Publ. 235, pp. 7-63.

Machel, H.G., Mason, R.A., Mariano, A.N., Mucci, A., 1991. Causes and Emission of Luminescence in Calcite and Dolomite. In: Barker, C. E., Kopp, O. C. (Eds.), Luminescence Microscopy and Spectroscopy: Qualitative and Quantitative Applications. SEPM Short Course Notes, 25. pp 9-25.

MacNaughton, R.B., Hagadorn, J.W., Dott Jr., R.H., 2019. Cambrian wave-dominated tidal-flat deposits, central Wisconsin, USA. Sedimentology. 66. 1643-1672.

Marshall, A.O., Emry, J.R., Marshall, C.P., 2012. Multiple Generations of Carbon in the Apex Chert and Implications for Preservation of Microfossils. Astrobiology 12, 160-166.

Marshall, C.P., Mar, G.L., Nicoll, R.S., Wilson, M.A., 2001. Organic geochemistry of artificially matured conodonts. Org. Geochem. 32, 1055-1071.

McCollom, T.M., Seewald, J.S., 2006. Carbon isotope composition of organic compounds produced by abiotic synthesis under hydrothermal conditions. Earth Planet Sci Lett. 243, 74-84.

McKirdy, D.M., Powell, T.G., 1974. Metamorphic Alteration of Carbon Isotopic Composition in Ancient Sedimentary Organic Matter: New Evidence from Australia and South Africa. Geology 2, 591-595.

Miller, B.L., 1941. LeHigh County Pennsylvania: Geology and Geography, Pennsylvania Geological Survey Bulletin, 4th Series C 39. Harrisburg, PA.

Monteverde, D.H., 1992. Bedrock geologic map of Sussex County, New Jersey, portions of the Culvers Gap and Lake Maskenozha quadrangles, New Jersey Geological Survey Geologic Map, 92-1.

Moore, C.H., 1989. Carbonate Diagenesis and Porosity, In: Moore, C. H. (Ed.), Developments in Sedimentology, 46, Amsterdam, Elsevier, pp. 46-338.

Morrow, D.W., 1982. Diagenesis II. Dolomite—Part II: Dolomitization Models and Ancient Dolostones. Geoscience Canada 9, 95-107.

Mueller, M., Igbokwe, O.A., Walter, B., Pederson, C.L., Riechelmann, S., Richter, D.K., Albert, R., Gerdes, A., Buhl, D., Neuser, R.D., Bertotti, G., Immenhauser, A., 2019. Testing the preservation potential of early diagenetic dolomites as geochemical archives. Sedimentology, 67, 849-881.

Mustard, J.F., Adler, M., Allwood, A., Bass, D.S., Beaty, D.W., Bell III, J.F., Brinckerhoff, W. B., Carr, M., Des Marais, D.J., Drake, B., Edgett, K.S., Eigenbrode, J., Elkins-Tanton, L.T., Grant, J.A., Milkovich, S. M., Ming, D., Moore, C., Murchie, S., Onstott, T.C., Ruff, S. W., Sephton, M.A., Steele, A., Treiman, A., 2013. Report of the Mars 2020 Science Definition

Team, 154 pp., posted July 2013, by the Mars Exploration Program Analysis Group (MEPAG) at http://mepag.jpl.nasa.gov/reports/MEP/Mars_2020_SDT_Report_Final.pdf.

Nordeng, S.H., Sibley, D.F., 1994. Dolomite stoichiometry and Ostwald's Step Rule. Geochim. Cosmochim. Acta 58, 191-196.

Oehlert, A.M., Lamb-Wozniak, K.A., Devlin, Q.B., Mackenzie, G.J., Reijmer, J.J.G., Swart, P.K., (2012). The stable carbon isotopic composition of organic material in platform derived sediments: implications for reconstructing the global carbon cycle. Sedimentology. 59, 319-335.

Oehlert, A.M., Swart, P.K., 2014. Interpreting carbonate and organic carbon isotope covariance in the sedimentary record. Nat. Commun. 5, 4672. https://doi.org/10.1038/ncomms5672.

Pasteris, J.D., Wopenka, B., 1991. Raman spectra of graphite as indicators of degree of metamorphism. Can. Mineral. 20, 1-9.

Pasteris, J.D., Wopenka, B., 2003. Necessary, but not sufficient: Raman identification of disordered carbon as a signature of ancient life. Astrobiology 3, 727-38.

Pina, C.M., Pimentel, C., Crespo, A., 2020. Dolomite cation order in the geological record. Chem. Geol. https://doi.org/10.1016/j.chemgeo.2020.119667.

Plummer, P.S., Gostin, V.A., 1981. Shrinkage cracks: desiccation or synaeresis. J. Sediment. Petrol. 51, 147-1156.

Pratt, B.R., James, N.P., Cowan, C.A., 1992. Peritidal carbonates. In: Walker, R. G., James, N. P. (Eds.), Facies Models – Response to Sea Level Change. Geological Association of Canada, pp. 303-322.

Radke, B.M., Mathis, R.L., 1980. On the Formation and Occurance of Saddle Dolomite. J. Sediment. Petrol. 50, 1149-1168.

Ramseyer, K., Amthor, J.E., Matter, A., Pettke, T., Wille, M., Fallick, A.E., 2013. Primary silica precipitate at the Precambrian/Cambrian boundary in the South Oman Salt Basin, Sultanate of Oman. Mar. Petrol. Geol. 39, 187-197.

Rao, V.P., Kessarkar, P.M., Krumbein, W.E., Krajewski, K.P., Schneider, R.J., 2003. Microbial dolomite crusts from the carbonate platform off western India. Sedimentology 50, 819-830.

Reeder, R.J., 1991. An Overview of Zoning in Carbonate Minerals. In: Barker, C. E., Kopp, O. C. (Eds.), Luminescence Microscopy and Spectroscopy: Qualitative and Quantitative Applications. SEPM Short Course Notes, 25. pp 77-82.

Reeder, R.J., Sheppard, C.E., 1984. Variation of lattice parameters in some sedimentary dolomites. Am. Mineral. 69, 520-527.

Richter, D.K., Götte, T., Götze, J., Neuser, R.D., 2003. Progress in application of cathodoluminescence (CL) in sedimentary petrology. Mineral. Petrol. 79, 127-166.

Ryan, B.H., Kaczmarek, S.E., Rivers, J.M., 2020. Early and pervasive dolomitization by near-normal marine fluids: New lessons from an Eocene evaporative setting in Qatar. Sedimentology. https://doi.org/10.1111/sed.12726.

Sanz-Montero, M.E., Rodríquez-Aranda, J.P., García del Cura, M.A., 2008. Dolomite-silica stromatolites in Miocene lacustrine deposits from the Duero Basin, Spain: the role of organotemplates in the precipitation of dolomite. Sedimentology 55, 729-750.

Schidlowski, M., 1988. A 3,800-million-year isotopic record of life from carbon in sedimentary rocks. Nature 333, 313-318.

Schopf, J.W., 1999. Cradle of Life: The Discovery of Earth’s Earliest Fossils. Princeton University Press, Princeton, New Jersey. 367 pp.

Schopf, J.W., Kudryavtsev, A.B., 2012. Biogenicity of Earth's earliest fossils: A resolution of the controversy. Godwana Research 22, 761-771.

Sena, C.M., John, C.M., Jourdan, A., Vandesignste, V., Manning, C., 2014. Dolomitization of Lower Cretaceous Peritidal Carbonates By Modified Seawater: Constraints From Clumped Isotopic Paleothermometry, Elemental Chemistry, and Strontium Isotopes. J. Sediment. Res. 84, 552-566.

Sharp, Z., 2007. Principles of Stable Isotope Geochemistry. Pearson Prentice Hall.

Siedlecka, A., 1978. Late Precambrian Tidal-Flat Deposits and Algal Stromatolites in the Batsfjord Formation, East Finnmark, North Norway. Sediment. Geol. 21, 277-310.

Sibley D., 1978. Dolomite textures. In: Middleton, G. V., Church, M. J., Coniglio, M., Hardie, L. A., Longstaffe, F. J. (Eds.), Encyclopedia of Sediments and Sedimentary Rocks. Encyclopedia of Earth Sciences Series. Springer, Dordrecht. https://doi.org/10.1007/3-540-31079-7_71.

Sibley, D.F., Gregg, J.M., 1987. Classification of Dolomite Rock Textures. J. Sed. Petrol. 57, 967-975.

Sibley D.F., 1991. Secular changes in the amount and texture of dolomite. Geology 19, 151-154.

Sijing, H., Keke, H., Jie, L., Yefang, L., 2014. The relationship between dolomite textures and their formation temperature: a case study from the Permian-Triassic of the Sichuan Basin and the Lower Paleozoic of the Tarim Basin. Pet. Sci. 11, 39-51.

Stead, R.J., Kodama, K.P., 1984. Paleomagnetism of the Cambrian Rocks of the Great Valley if East Central Pennsylvania: Fold Test Constraints on the Age of Magnetization¸ Plate reconstruction. In: Van der Voo, R., Scotese, C. R., Bonhommet, N. (Eds.), Paleozoic paleomagnetism: Interim report of the Working Group 2 on Phanerozoic Plate Motions and Orogenesis. Washington, D. C.: American Geophysical Union. pp 120-130.

Strauss, H., Beukes, N.J., 1996. Carbon and sulfur isotopic compositions of organic carbon and pyrite sediments from the Transvaal Supergroup, South Africa. Precambr. Res. 79, 57-71.

Sugitani, K., Grey, K., Allwood, A., Nagaoka, T., Mimura, K., Minami, M., Marshall, C.P., Van Kranendonk, M.J., Walter, M.R., 2007. Diverse microstructures from Archaean chert from the Mount Goldsworthy–Mount Grant area, Pilbara Craton, Western Australia: Microfossils, dubiofossils, or pseudofossils? Precambr. Res. 158(3-4), 228-262.

Summons, R.E., Amend, J.P., Bish, D., Buick, R., Cody, G.D., Des Marais, D.J., Dromart, G., Eigenbrode J.L., Knoll, A.H., Sumner, D.Y., 2011. Preservation of Martian Organic and Environmental Records: Final Report of the Mars Biosignature Working Group. Astrobiology. 11, 157-181.

Swart, P.K., 2015. The geochemistry of carbonate diagenesis: The past, present, and future. Sedimentology. 62, 1233-1304.

Tilley, C. 1924. The Facies Classification of Metamorphic Rocks. Geological Magazine 61, 167-170.

Tucker, M., Wright, V.P., 1990. Carbonate Sedimentology. Blackwell Scientific Publications, Oxford.

Vahrenkamp, V.C., Swart, P.K., 1990. New distribution coefficient for incorporation of strontium into dolomite and its implications for the formation of ancient dolomites. Geology 18, 387-391.

Van Kranendonk, M.J., Webb, G.E., Kamber, B.S., 2003. Geological and trace element evidence for a marine sedimentary environment of deposition and biogenicity of 3.45 Ga stromatolitic carbonates in the Pilbara Craton, and support for a reducing Archaean ocean. Geobiology 1, 91-108.

Warren, J., 2000. Dolomite: occurrence, evolution, and economically important associations. Earth-Sci. Rev. 52, 1-81.

Weller, S., 1903. The Paleozoic faunas: New Jersey Geological Survey Report on Paleontology, 3.

Williford, K. H., Farley, K. A., Stack, K. M, Allwood, A. B., Beaty, D., Beegle, L. W., … et al., 2018. Chapter 11 - The NASA Mars 2020 Rover Mission and the Search for Extraterrestrial Life. From Habitability to Life on Mars, 275–308.

Wilson J.L., 1975. Carbonate Facies in Geologic History, Springer-Verlag, New York.

Witte, R.W., Monteverde, D.H., 2012. Geologic History of New Jersey's Valley and Ridge Physiographic Province, New Jersey Geological and Water Survey Information Circular, Trenton, NJ.

Wopenka, B., Pasteris, J.D., 1993. Structural characterization of kerogens to granulite-facies graphite: Applicability of Raman microprobe spectroscopy. Amer. Miner. 78, 533-557.

Zhang, J., Hu, W., Qian, Y., Wang, X., Cao, J., Zhu, J., Li, Q., Xie, X., 2009. Formation of saddle dolomites in Upper Cambrian carbonates, western Tarim Basin (northwest China): Implications for fault-related fluid flow. Mar. Petrol. Geol. 26, 1428-1440.

TABLES

Sample ID	Sample Description	Method				
		XRD	EPMA	CL	IRMS	Raman*
A18	dolarenite mudcracks	x				
A17	feldspathic dolarenite tidal channel deposit	x				
A16	dolosiltite domal stromatolite	x	x	x	x	x
A15a	chert lens	x			x	
B14	oolitic dolosiltite	x	x	x	x	
B13	oolitic dolosiltite	x			x	
B12a	oolitic dolarenite	x	x	x	x	x
B11	dolarenite	x	x	x	x	
B10	oolitic dolarenite	x	x	x	x	
B9	oolitic dolosiltite	x			x	
A8	dolosiltite	x			x	
A7	oolitic dolosiltite	x	x	x	x	x
A6	feldspathic dolosiltite disk	x			x	
A5	oolitic dolosiltite thrombolite	x		x	x	x
A4	dolosiltite	x			x	
A3	dolosiltite with microstyolites	x	x	x	x	
A2	dolosiltite with solution seams	x			x	
A1	dolosiltite with solution seams			x	x	
B15b	dolomitic chert lens	x				
*12b	oolitic dolarenite	x				
*12c	oolitic dolarenite	x				
*12d	oolitic dolarenite	x				

x denotes sample analyzed

* denotes all samples analyzed by method but final representative samples used in paper are marked here

A,B,* denote sampling points marked on Fig. 3

Table 1. Table of methods used in study with the samples analyzed using different methods.

Sample ID	Sample Description	Degree of Cation Order (d_{015}/d_{110})	Stoichiometry					
			d_{104}-spacing	P-XRD CaCO3 (mol%)	Mg/Ca	EPMA (Mg/Ca) Micritic	Zoned	Saddle
A18	dolarenite mudcracks	0.654	2.890	51.23	0.95	-	-	-
A17	feldspathic dolarenite tidal channel deposit	0.604	2.888	50.69	0.97	-	-	-
A16	dolosiltite domal stromatolite	0.599	2.886	50.00	1.00	1.02	1.02	0.99
A15a	chert lens	n/a	n/a	n/a	n/a	-	-	-
B14	oolitic dolosiltite	0.659	2.893	52.33	0.91	1.02	n/a	0.97
B13	oolitic dolosiltite	0.619	2.893	52.33	0.91	-	-	-
B12a	oolitic dolarenite	0.848	2.893	52.33	0.91	1.03	1.04	n/a
B11	dolarenite	0.989	2.884	49.33	1.03	1.03	1.03	n/a
B10	oolitic dolarenite	0.640	2.893	52.33	0.91	1.03	n/a	n/a
B9	oolitic dolosiltite	0.491	2.893	52.33	0.91	-	-	-
A8	dolosiltite	0.375	2.893	52.33	0.91	-	-	-
A7	oolitic dolosiltite	0.900	2.893	52.33	0.91	1.02	1.03	n/a
A6	feldspathic dolosiltite disk	n/a	2.888	50.67	0.97	-	-	-
A5	oolitic dolosiltite thrombolite	0.596	2.885	49.67	1.01	-	-	-
A4	dolosiltite	0.737	2.894	52.67	0.90	-	-	-
A3	dolosiltite with microstyolites	0.683	2.893	52.33	0.91	1.02	1.04	n/a
A2	dolosiltite with solution seams	0.363	2.894	52.67	0.90	-	-	-
A1	dolosiltite with solution seams	-	-	-	-	-	-	-
B15b	dolomitic chert lens	n/a	2.854	39.33	1.54	-	-	-
*12b	oolitic dolarenite	0.656	2.889	51.10	0.96	-	-	-
*12c	oolitic dolarenite	0.772	2.891	51.61	0.94	-	-	-
*12d	oolitic dolarenite	0.788	2.890	51.35	0.95	-	-	-

dolosiltite = silt sized grains (5 µm - 63 µm)
dolarenite = sand sized grains (63 µm - 2 mm)
n/a denotes no data from analysis
- denotes the sample was not analyzed
A,B,* denote sampling points marked on Fig. 3

Table 2. Stoichiometry and cation order within samples listed from bottommost to topmost sampled strata, *12d to A18, respectively. Cation order ranges from 0.36 – 0.99 and indicates the Allentown dolomite is poorly to well ordered. Values from XRD d-spacing, converted to mol%. and EPMA Mg/Ca ratios show that bulk dolostone samples from the Allentown range from near stoichiometric (low Ca-excess) to stoichiometric (50 mol% $CaCO_3$). EPMA Mg/Ca ratios for individual dolomite phases show microspar and zoned dolomite are stoichiometric and saddle dolomite is near stoichiometric (low Ca-excess).

			Cluster		
	I_D/I_G	**G-FWHM**	**G position**	**D-FWHM**	**D position**
Average	1.00	45.01	1600.54	68.42	1334.28
SD	0.01	3.48	5.29	13.91	4.11
Relative SD	1.40	7.74	0.33	20.33	0.31
Min	0.96	36.43	1594.66	49.06	1327.14
Max	1.02	50.33	1609.00	83.02	1339.00
Range	0.05	13.90	14.34	33.96	11.86
			Gaussian fit		
	I_D/I_G	**G-FWHM**	**G position**	**D-FWHM**	**D position**
Average	1.02	44.21	1599.34	47.29	1335.40
SD	0.18	7.91	5.69	16.54	7.92
Relative SD	17.59	17.90	0.36	34.98	0.59
Min	0.70	25.17	1591.26	19.38	1321.59
Max	1.45	52.83	1608.52	75.88	1347.17
Range	0.75	27.66	17.26	56.50	25.58

Table 3. Average D and G band values from microspar dolomite phase within samples A16, A5, A7, B11, and B12a obtained from the cluster and Gaussian fit methods showing overall comparable values among both peak processing methods used. The variance in the Gaussian fitted spectra compared to the spectra from the cluster analysis may be due to more noise in the final spectrum of the background-subtracted Gaussian fitted peaks related to difference in the number of points selected by hand versus selected by computer in the cluster process.

Sample ID	Sample Type	Temperature °C	T(°C) range
A16	Stromatolite	323.65 342.80 367.29	324°C - 367°C (345°C avg.)
B12	Oolitic Dolarenite	372.53	362°C - 373°C (368°C avg.)
B11	Dolarenite	370.71	
A7	Oolitic Dolosiltite	361.77	
A5	Thrombolite	312.43 307.91 308.67 299.52 301.76 301.73	300°C - 312°C (305°C avg.)

Table 4. Derived temperatures showing temperature variations as they appear in Fig. 14.

FIGURES

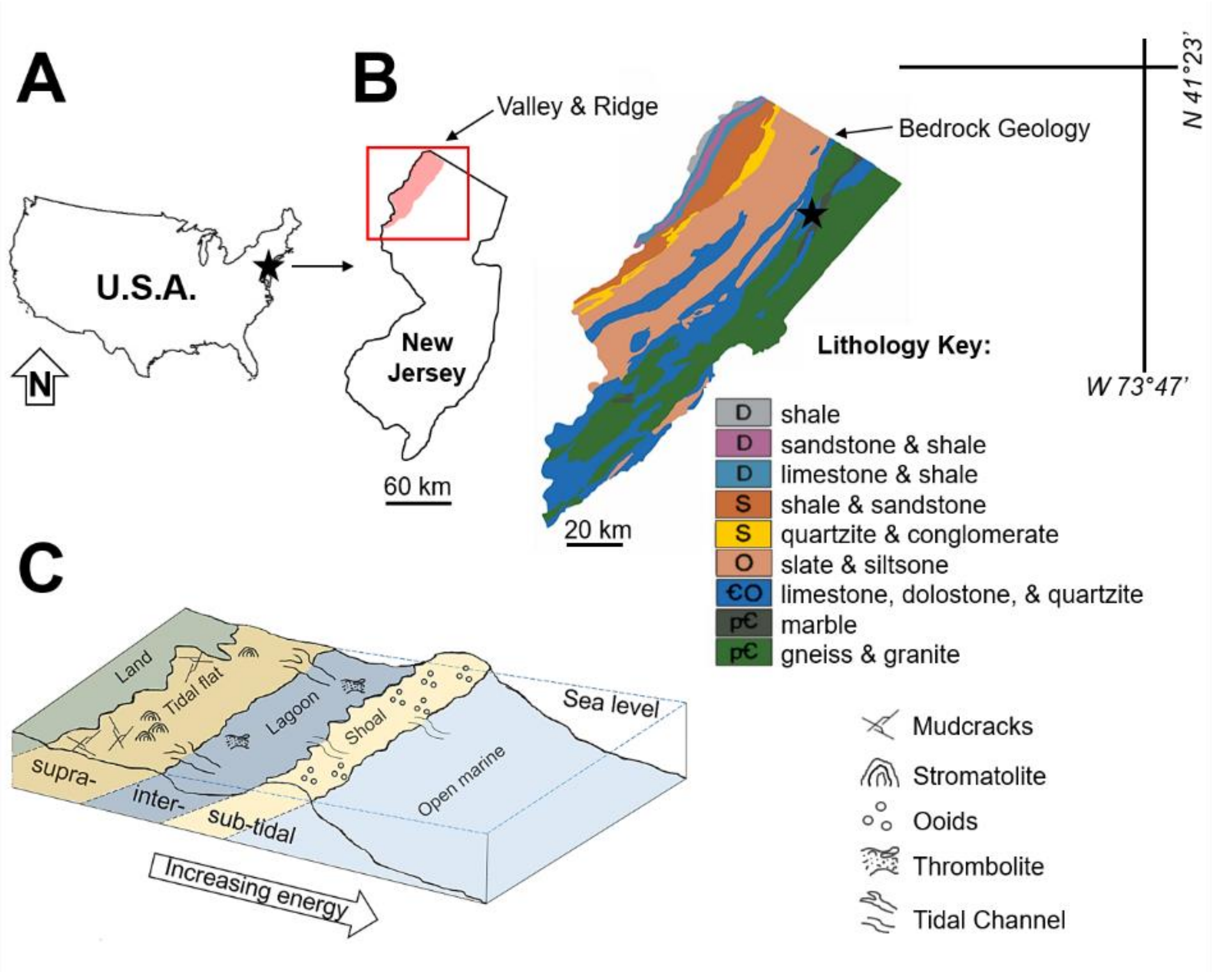

Fig. 1. Geologic map and sampling location. (A) Location of New Jersey (NJ) (marked by star) within the United States of America (U.S.A). (B) The Cambrian to Middle Ordovician Kittatinny Supergroup (blue lithology) of the Valley and Ridge Physiographic Providence in NJ (red shaded area within red box of inset NJ map). Location of the studied Allentown Formation outcrop (marked by star) in Hamburg, NJ. Modified from Witte and Monteverde (2012). (C) Reconstruction of paleoenvironment based on outcrop observations in this study. Modified from Pratt et al. (1992).

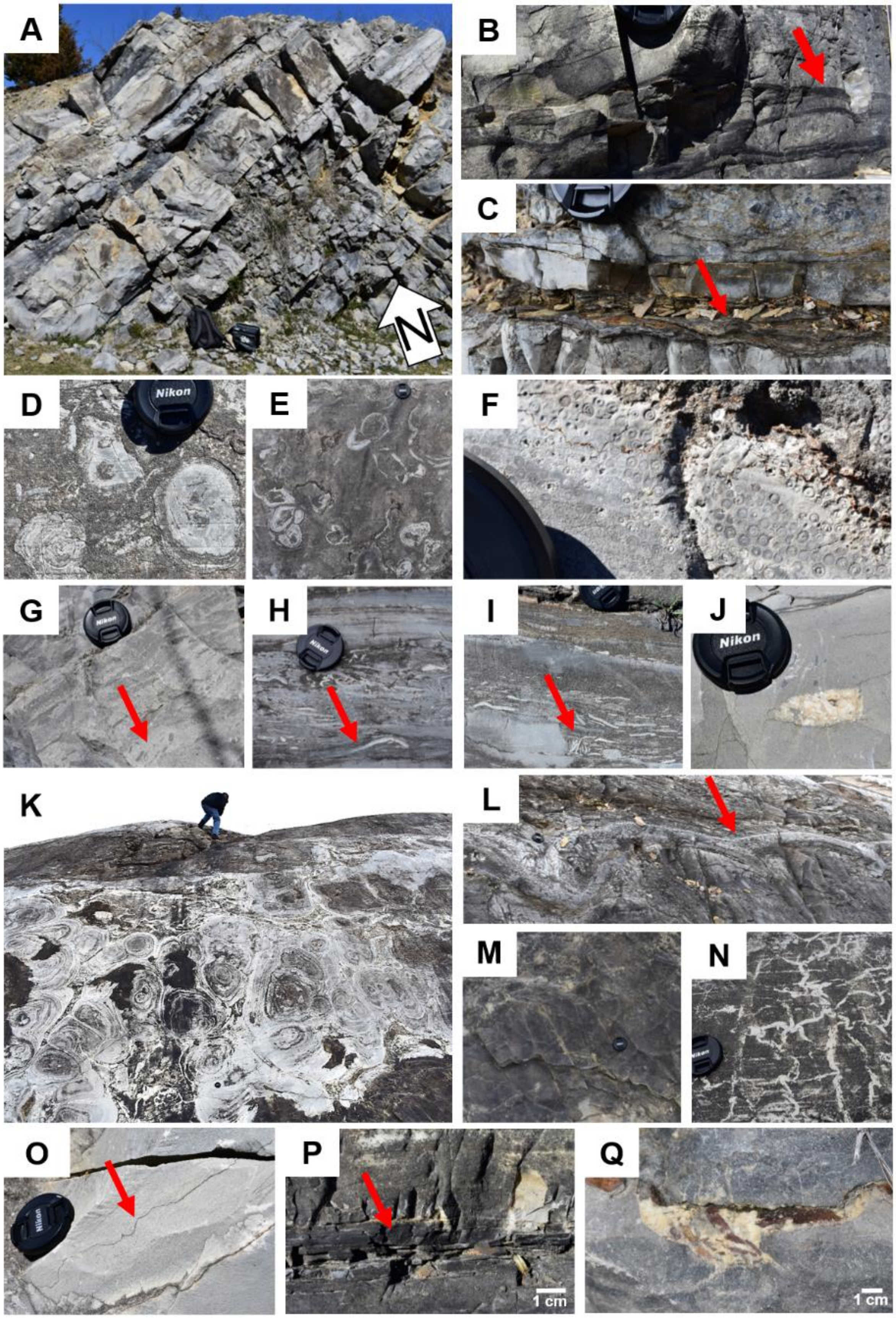

1164

Fig. 2. (A) Side view of formation with tilted layers dipping 44° NW. (B) Dolosiltite intercalated with solution seams. (C) Brown crinkled layer (red arrow) marks the top of thrombolites (D) Small stromatolite heads. (E) Ripped up stromatolite heads. (F) Ooid grainstone. (G) Dark grey rip-up clasts. (H) Edgewise conglomerates. (I) Jumbled intraclasts. (J) Large vug filled with coarse-grained dolomite. (K) Top of formation with glacially smoothed domal stromatolites (L) convex upward shape of stromatolites from NE side of outcrop. (M) Mudcracks and (N) syneresis cracks visible from top of formation. (O) Wavy stylolite parallel to bedding. (P) Black chert lens. (Q) Collapsed stylolite material into coarse-grained dolomite filled vug. Nikon camera lens (5.5 cm radius) used for scale.

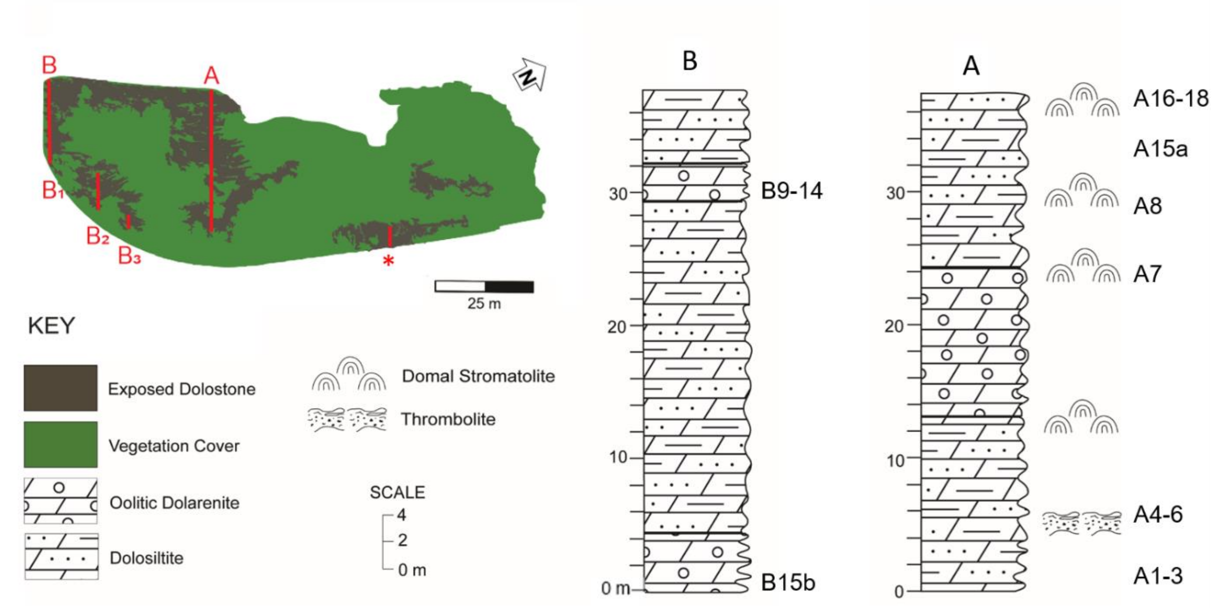

Fig. 3. Stratigraphic columns made from sampled transects. Column B is exact bedding thickness measured along B1, B2 and B3 (marked red on outcrop figure). Column A is estimated thickness along glacially smoothed bedding measured along A (marked red). Asterisk (*) marks area of samples 12b-d collection (Table 2). Outcrop figure modified from aerial Google Earth imagery. Note the lateral differences in both columns and lack of microbial structures observed at Column B. Sampling points are marked by sample number to the right or each column to show where each sample type was collected.

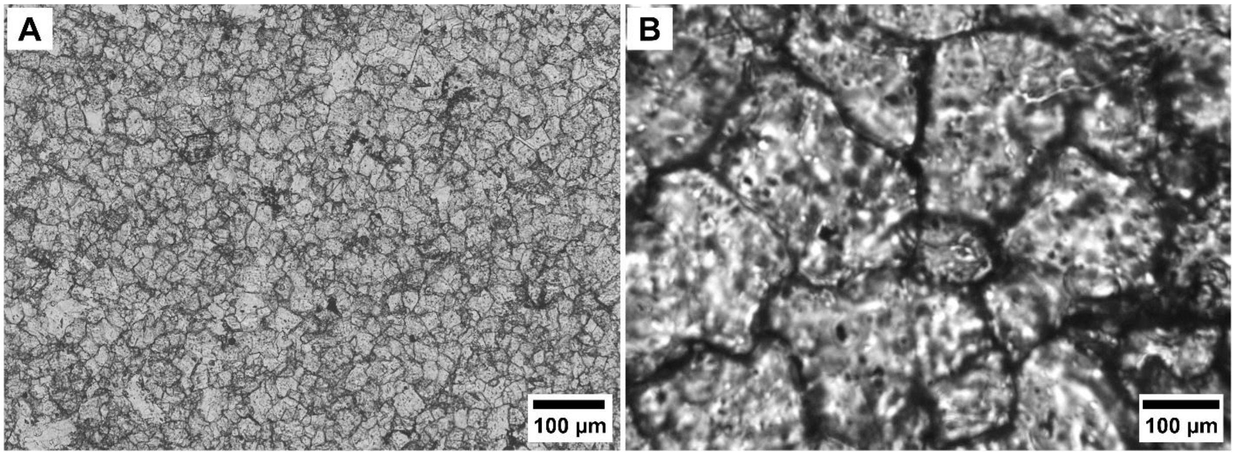

Fig. 4. Nonplanar texture of microspar dolomite. (A) Plane polarized light (PPL) photomicrograph from thin section of sample B11. (B) Transmitted confocal light micrograph of the same sample from (A) taken with confocal Raman microscope.

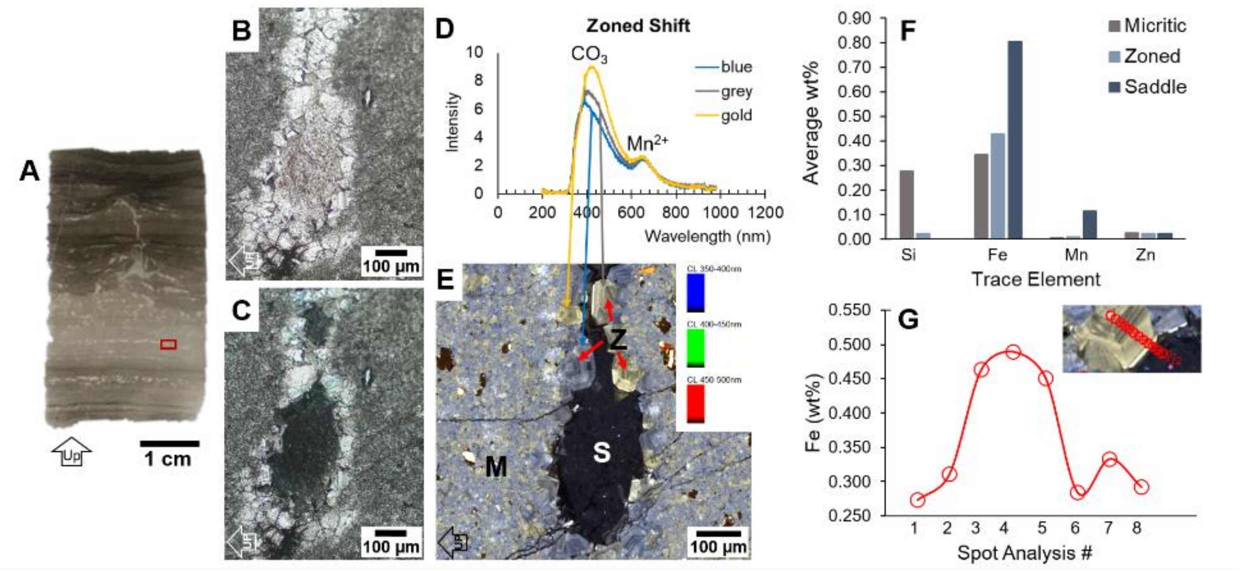

Fig. 5. CL and EPMA results. (A) Thin section of domal stromatolite (A16). Red box indicates mapped area in (E). (B) PPL photomicrograph of fenestral pore from sample (A). (C) Cross polarized light (XPL) photomicrograph of (B). (D) Characteristic spectra of luminescence colors showing a peak shift at CO_3. (E) CL map showing three phases of dolomite: microspar (M), zoned (Z), and saddle (S) within sample (A). (F) EPMA spot analyses across each phase of dolomite within sample (A) showing the dolomitizing fluid compositional changes. (G) EPMA spot analysis across zoned dolomite within sample (A) reveals dark zonation bands are Fe-enriched.

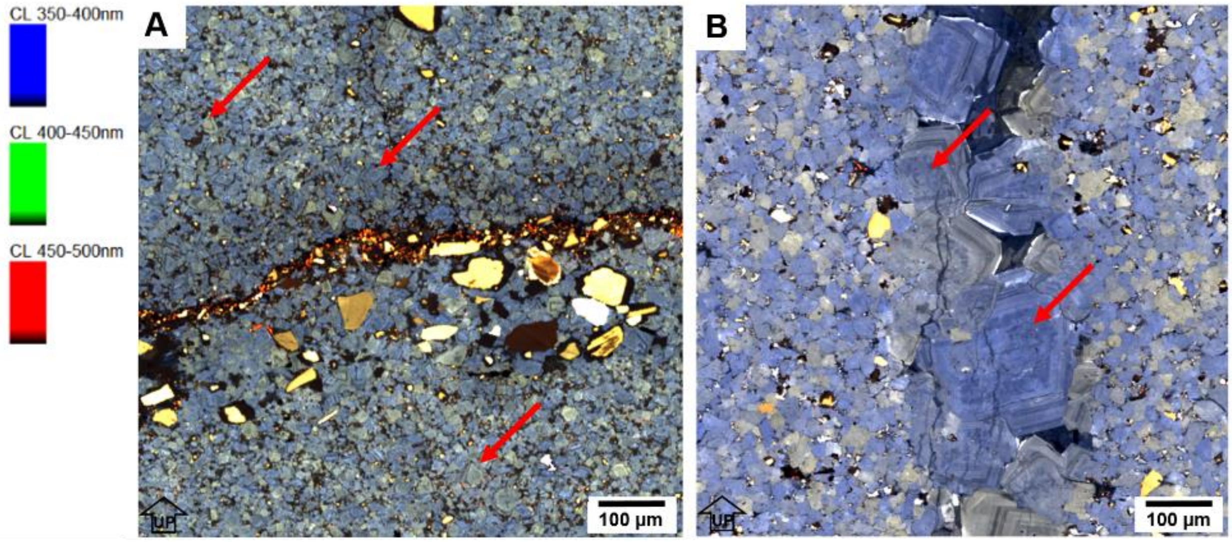

Fig. 6. (A) CL map of microstylolite from dolosiltite sample A3 showing zoned rhombohedral dolomite in pores of the microspar dolomite matrix (red arrows). Numerous feldspars (larger yellow-brown grains) can be seen near the solution seam. (B) CL map of vertical microfracture in dolarenite sample B11 showing zoned dolomite that lines and fills the microfracture. The rhombohedral dolomite cores appear patchy in CL (red arrows).

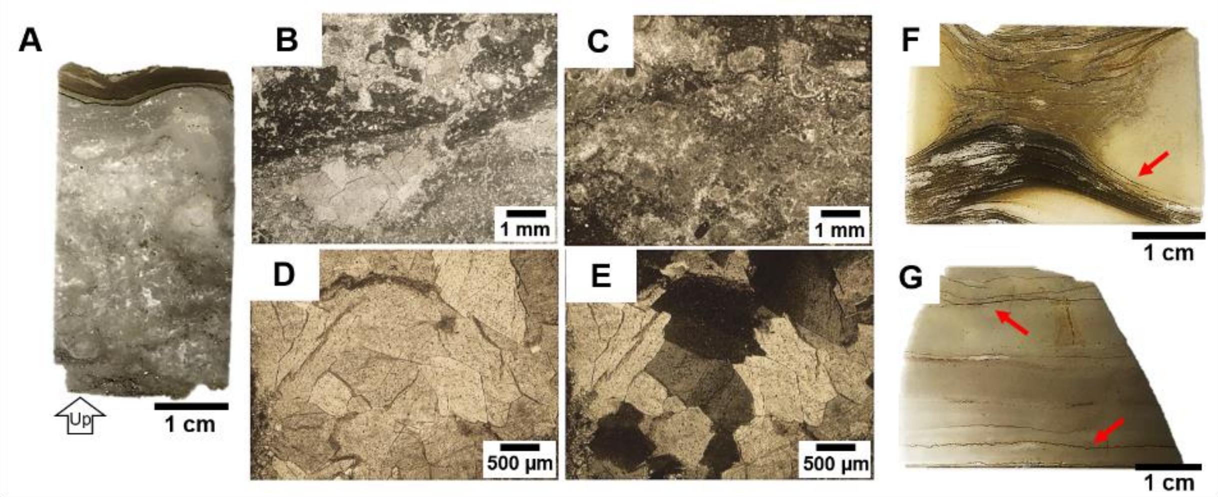

Fig. 7. Subtidal lagoonal facies microtextures**.** (A) Thin section of thrombolite sample. PPL photomicrographs of: (B) clotted structure and large saddle dolomite-filled vug, (C), clotted thrombolite structure, and (D) large saddle dolomite filled vug indicative of burial dolomitization. (E) XPL photomicrograph of (D) shows sweeping extinction characteristic of saddle dolomite. (F) Thin section of dolosiltite sample (A1) with wispy solution seams (red arrow). (G) Thin section of dolosiltite sample (A3) with microstylolites (red arrows).

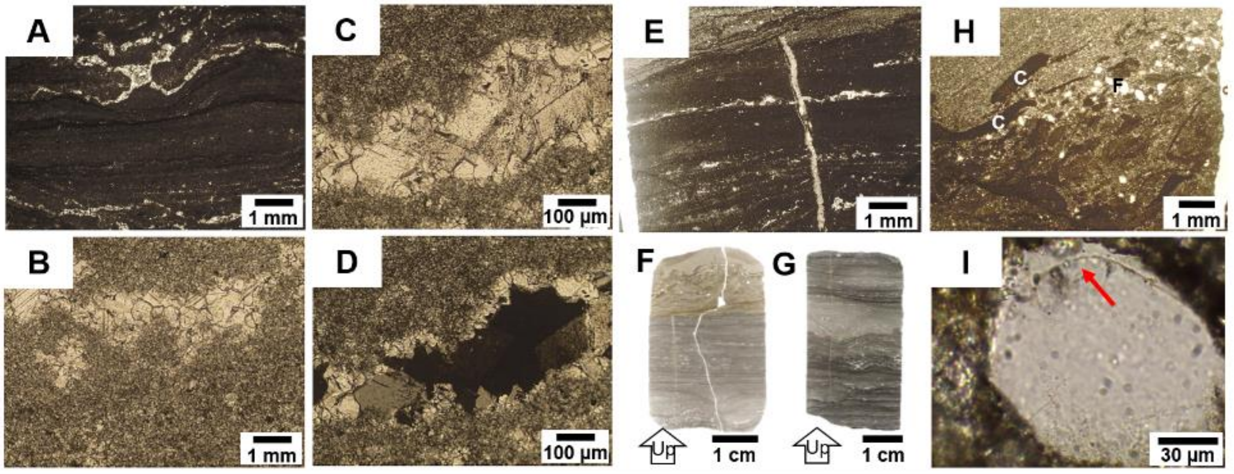

Fig. 8. Tidal flat stromatolitic facies microtextures. Thin sections of the top (F) and bottom (G) of a large domal stromatolite sample. with corresponding PPL photomicrographs: (H) rip-up clasts (marked C) and feldspars (marked F) within topmost portion of dome (in F) indicate a tidal channel deposit; (I) Confocal Raman micrograph from (H) of an orthoclase overgrowth rim (red arrow) indicate thermal alteration from; (E) preservation of primary fenestral porosity that is crosscut by secondary microfracture porosity, evidence for early, near-surface dolomitization; (A) Very fine laminae of finely crystalline dolomite, common to tidal flat stromatolites. Fenestrae (light colored areas in image) is filled with zoned and saddle dolomite; (B) Microspar dolomite and coarser-grained zoned dolomite-filled fenestrae; (C) Zoned and saddle dolomite-filled fenestrae surrounded by microspar. (D) XPL photomicrograph of (C).

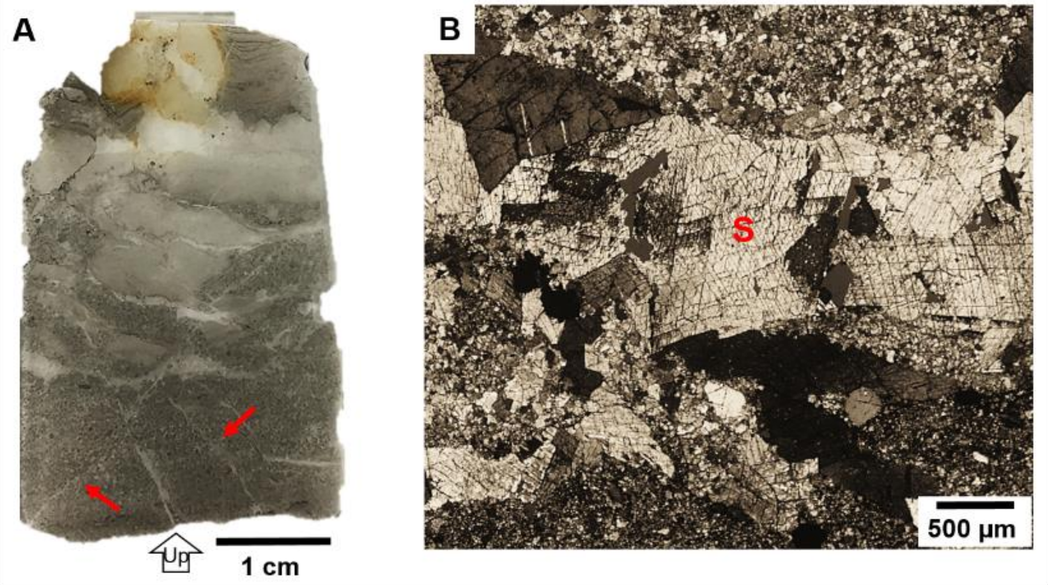

Fig. 9. Randomly oriented fractures in sample B14. (A) Thin section of sample B14 with non-vertical fractures (red arrows). (B) XPL photomicrograph of saddle shaped dolomite (marked S) infilling a fracture in (A).

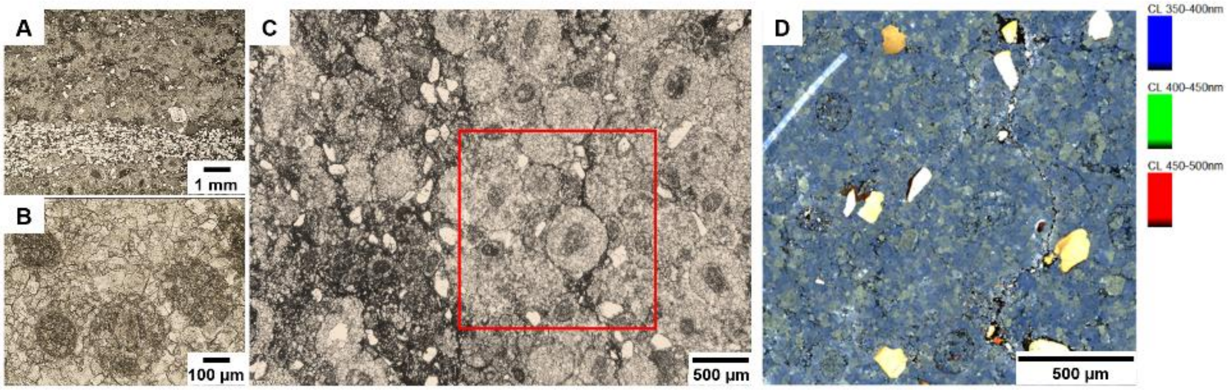

Fig. 10. Oolitic grainstone microtextures observed in thin sections. (A) PPL photomicrograph of ooids (sample B10) with a finer-grained siliceous layer near the bottom of the image (white area). (B) Photomicrograph in ppl of ooids from (A) showing dolomite replacement. (C) PPL photomicrograph of CL mapped area (red box) in (D). (D) CL map showing characteristic violet luminescence. Bright white and yellow grains are feldspars.

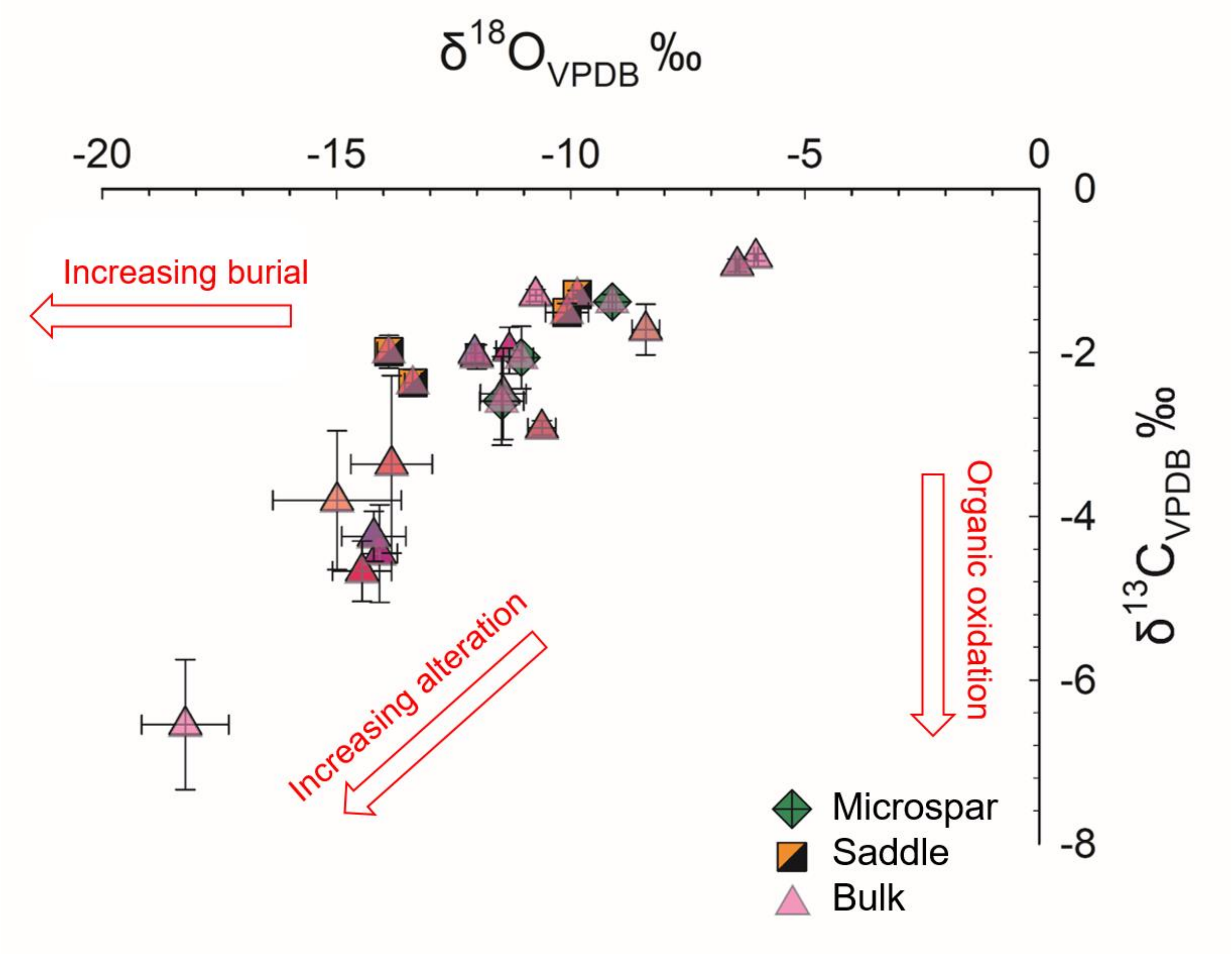

Fig. 11. The $\delta^{13}C_{dolo}$ and $\delta^{18}O_{dolo}$ compositions measured from bulk samples, and micro-drilled microspar and saddle dolomites. Overall alteration trends are marked by red arrows. Modified from Allan and Wiggins (1993). The low isotopic values trend is indicative of thermal alteration from burial dolomitization.

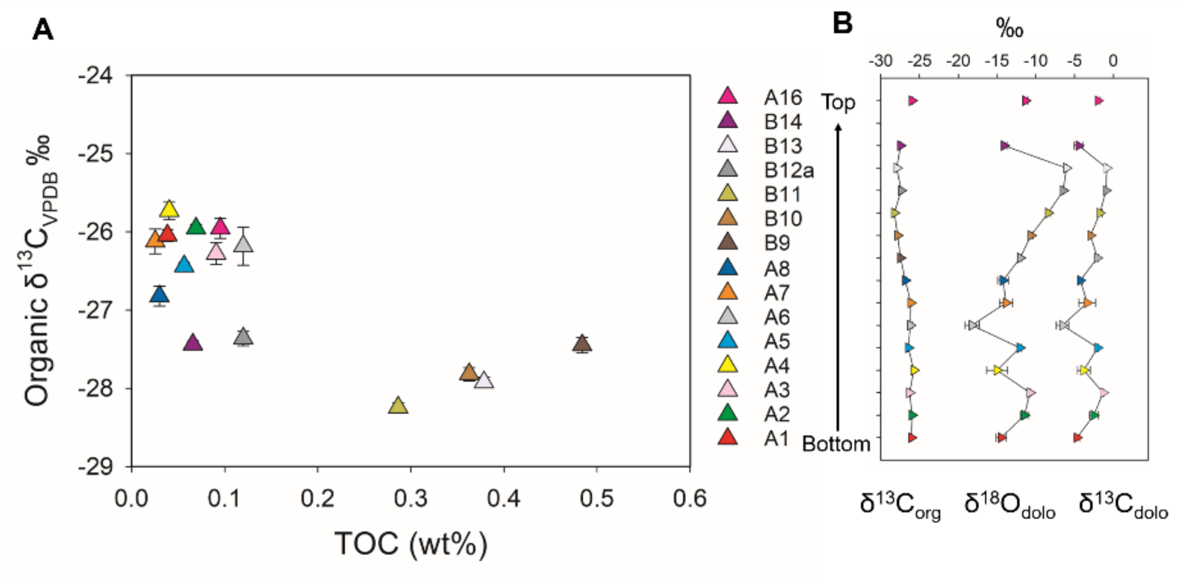

Fig. 12. Graphs showing diagenetic alteration modes in $\delta^{13}C_{org}$, $\delta^{18}O_{dolo}$, and $\delta^{13}C_{dolo}$ isotopic trends and TOC**.** (A) Bi-plot of TOC wt% and $\delta^{13}C_{org}$ ‰ values. (B) The $\delta^{13}C_{org}$, $\delta^{18}O_{dolo}$, and $\delta^{13}C_{dolo}$ isotopic trends across the outcrop reveal coupled $\delta^{18}O_{dolo}$ and $\delta^{13}C_{dolo}$ values, but $\delta^{18}O_{dolo}$ and $\delta^{13}C_{dolo}$ are decoupled with $\delta^{13}C_{org}$ isotopes. TOC error bars are obscured by symbols and are listed in Table S2 in supplementary material.

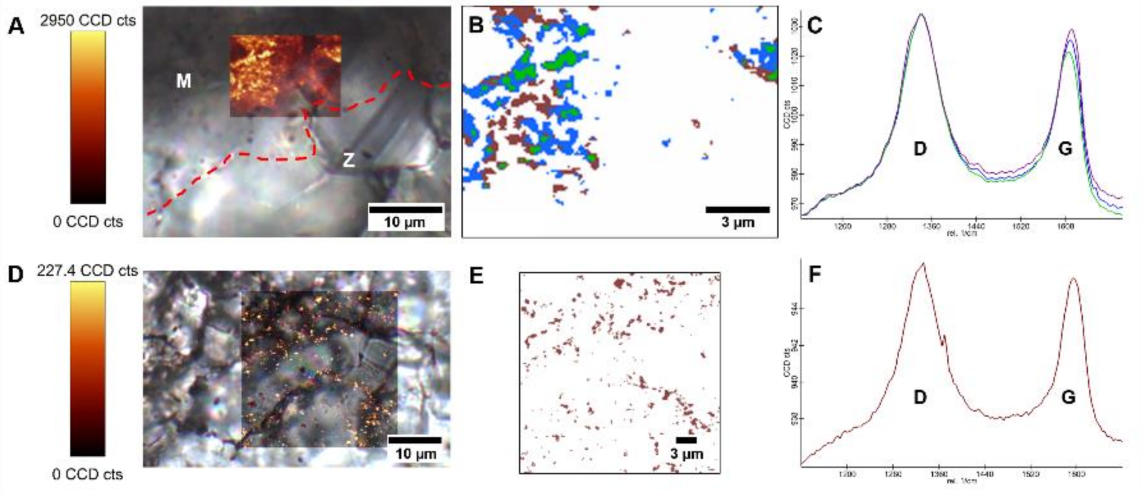

Fig. 13. Raman cluster method example. (A) Transmitted light micrograph of stromatolite sample (A16) with overlay of Raman mapped D and G bands area. Bright yellow spots within the Raman map indicate spatial distribution of D and G bands before the cluster analysis. D and G bands are associated only with the microspar phase of dolomite (marked M) but not the zoned phase (marked Z). Note the z-depth of confocal images reveals the transition from M to Z, where M overlays Z near the boundary between phases. The boundary determined from surface (z-depth=0) is marked with red dotted line. (B) Raman map after cluster analyses showing differences in D and G bands averages and their spatial distribution. (C) overlay of D and G bands showing slight peak shift of G band which may indicate different levels of crystallinity. (D) Transmitted light micrograph of oolitic sample (B12a) with overlay of Raman mapped D and G bands area. Bright yellow spots within the Raman map indicate spatial distribution of D and G bands within the microspar dolomite before the cluster analysis. (E) Raman map after cluster analyses showing one type of D and G bands. (F). Raman spectra of D and G bands which exhibits different peak parameters than the stromatolite sample in (C).

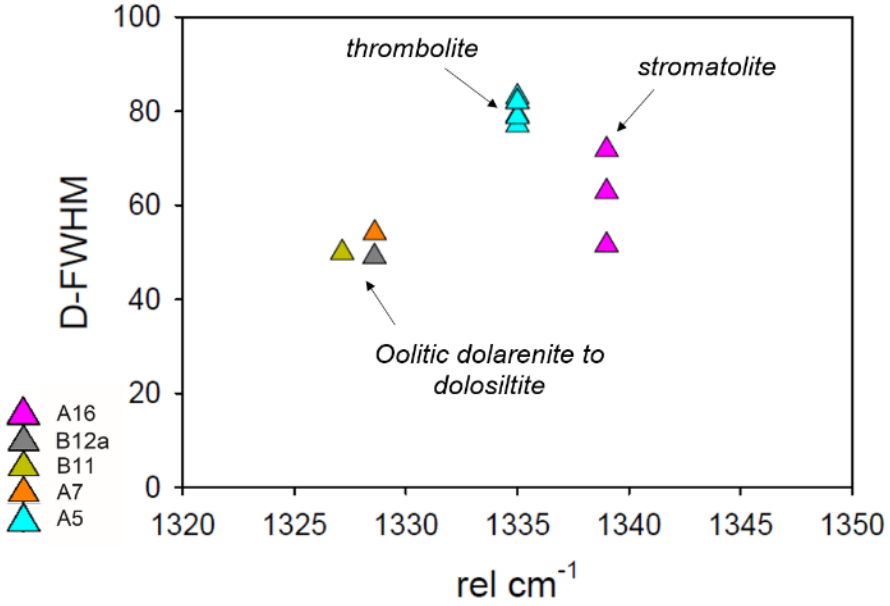

Fig. 14. Raman D band characteristics from cluster method, reveals that the samples group together by general facies type.

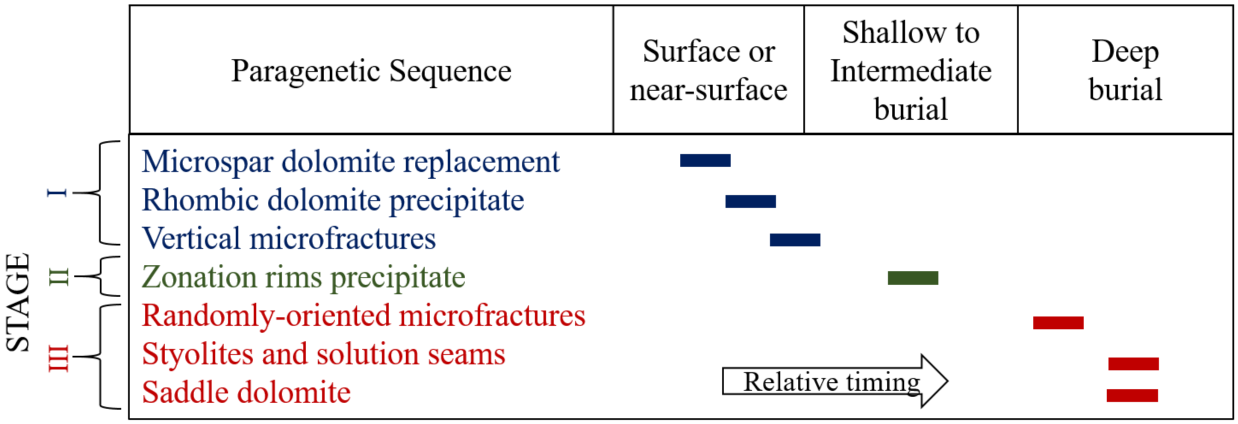

Fig. 15. Interpreted paragenetic sequence showing the formation of each dolomite phase with increasing burial depth. Modified from Hips et al. (2015).